Consequences of Exchange-Site Heterogeneity and Dynamics on the UV-Visible Spectrum of Cu-Exchanged SSZ-13

Hui Li,[†,⊥] Christopher Paolucci,[†,‡,⊥] Ishant Khurana,[¶] Laura N. Wilcox,[¶] Florian Göltl,[§] Jonatan D. Albarracin Caballero,[¶] Arthur J. Shih,[¶] Fabio H. Ribeiro,[¶] Rajamani Gounder,[*,¶] and William F. Schneider[*,‖]

†*Department of Chemical and Biomolecular Engineering, University of Notre Dame, 182 Fitzpatrick Hall, Notre Dame, IN 46556, USA*

‡*Department of Chemical Engineering, University of Virginia, 102 Engineer's Way, Charlottesville, VA 22904, USA*

¶*Charles D. Davidson School of Chemical Engineering, Purdue University, 480 Stadium Mall Drive, West Lafayette, IN 47907, USA*

§*Department of Chemical and Biological Engineering, University of Wisconsin-Madison, 1415 Engineering Drive, Madison, WI 53706, USA*

‖*Department of Chemical and Biomolecular Engineering, University of Notre Dame 182 Fitzpatrick Hall, Notre Dame, IN 46556, USA*

⊥*Contributed equally to this work*

E-mail: rgounder@purdue.edu; wschneider@nd.edu

Abstract

The speciation and structure of Cu ions and complexes in chabazite (SSZ-13) zeolites, which are relevant catalysts for nitrogen oxide reduction and partial methane

oxidation, depend on material composition and reaction environment. Ultraviolet-visible (UV-Vis) spectra of Cu-SSZ-13 zeolites synthesized to contain specific Cu site motifs, together with ab initio molecular dynamics and time-dependent density functional theory calculations, were used to test the ability to relate specific spectroscopic signatures to specific site motifs. Geometrically distinct arrangements of two framework Al atoms in six-membered rings are found to exchange Cu^{2+} ions that become spectroscopically indistinguishable after accounting for the finite-temperature fluctuations of the Cu coordination environment. Nominally homogeneous single Al exchange sites are found to exchange a heterogeneous mixture of $[CuOH]^+$ monomers, O- and OH-bridged Cu dimers, and larger polynuclear complexes. The UV-Vis spectra of the latter are sensitive to framework Al proximity, to precise ligand environment, and to finite-temperature structural fluctuations, precluding the precise assignment of spectroscopic features to specific Cu structures. In all Cu-SSZ-13 samples, these dimers and larger complexes are reduced by CO to Cu^+ sites at 523 K, leaving behind isolated $[CuOH]^+$ sites with a characteristic spectroscopic identity. The various mononuclear and polynuclear Cu^{2+} species are distinguishable by their different responses to reducing environments, with implications for their relevance to catalytic redox reactions.

1 Introduction

Copper ions exchanged onto zeolites are implicated as active sites for the selective catalytic reduction of nitrogen oxides,[1–10] oxidation of NO to NO_2,[11,12] decomposition of NO and N_2O,[13–16] and partial methane oxidation to methanol.[17–33] These Cu ions are associated with charge-compensating AlO_4^- tetrahedral sites that are distributed throughout the zeolite lattice. Because these Al substitutions are not ordered under typical zeolite synthesis conditions, a given framework and macroscopic Si/Al ratio will present a heterogeneous distribution of microscopic Al site ensembles, each of which provides a distinct exchange environment for a Cu ion. The precise Cu species and their relative densities in a given

material are thus functions of framework topology,[34–37] of the density and underlying distribution of framework Al (Si/Al), of the Cu loading (Cu/Al), and even of the protocols used to introduce Cu onto the zeolite supports.[38–44] Further, multiple Cu ion site motifs may be of similar free energy at a given Al site or ensemble, and at finite temperatures these motifs may interchange at timescales relevant to observation or to catalytic turnover.[45–47] Given these many sources of structural diversity, assignment of spectroscopic features to specific Cu motifs in a heterogeneous solid is a non-trivial endeavor, but a critical one to make connections between local structure and catalytic function.

One strategy to reduce this complexity is to intentionally synthesize zeolites with framework Al distributions that present one or a few distinct Al site ensembles. This strategy is particularly promising for zeolites of relatively high symmetry, such as the chabazite (SSZ-13) framework that is composed of a single symmetry-distinct tetrahedral site. SSZ-13 samples synthesized using only organic N,N,N-trimethyl-1-adamantylammonium ($TMAda^+$) structure-directing cations nominally contain only isolated framework Al sites,[39] and are found to contain predominantly $[CuOH]^+$ ions after aqueous Cu ion exchange and high temperature (>473 K) oxidation, based on titrimetric analysis and vibrational and X-ray spectroscopies.[38] In contrast, SSZ-13 samples synthesized in the presence of $TMAda^+$ and Na^+ as co-structure-directing cations[39] contain detectable fractions of paired Al sites in 6-membered rings (6MR). After Cu ion exchange and high temperature oxidative treatment, these paired Al sites are observed to preferentially host Cu^{2+} ions (Z_2Cu) before isolated Al sites are occupied by $[CuOH]^+$ ions (ZCuOH).[38] Z_2Cu and ZCuOH are expected to contribute differently to ultraviolet-visible (UV-Vis) absorption spectra based on ligand-field arguments and density functional theory (DFT) calculations, consistent with d-d transition and ligand-to-metal charge transfer (LMCT) features in experimentally-measured UV-Vis spectra that are observed to change with Cu content in Cu-SSZ-13 samples.[6,48–50]

These single Cu species may coexist with dimeric or higher nuclearity Cu clusters. Oxygen-bridged Cu dimers are well established to be present and quantifiable with CO

temperature programmed reduction,[15] to be plausible active sites for NO and N_2O decomposition[14,15,51–53] and partial CH_4 oxidation in Cu-exchanged zeolites,[17,30,33,54–62] including Raman[63,64] and UV-Vis[14,55] spectroscopic observations and CO temperature programmed reduction to quantify such sites. In Cu-SSZ-13 samples of certain composition (Si/Al=5, Cu/Al=0.3-1.6), oxygen-bridged Cu dimers and larger Cu oxide aggregates are detected by X-ray spectroscopy and are the dominant active sites for NO oxidation to NO_2 under dry conditions.[11] UV-Vis spectra of certain Cu-SSZ-13 samples (Si/Al=13, Cu/Al=0.45) following high temperature O_2 treatment show features consistent with those for oxygen-bridged Cu dimers,[48] and these features disappear upon reduction with CH_4,[18,50] implicating them as active sites for partial methane oxidation. The precise relationship between sample composition and treatment history, and the numbers and structures of Cu dimers or larger aggregates formed, however, remains less well resolved than such relationships for monomeric Cu sites in Cu-SSZ-13.

Here, we report UV-Vis spectra of model Cu-SSZ-13 zeolites prepared to contain predominantly Z_2Cu or ZuOH sites, by virtue of their different framework Al arrangements and elemental compositions. We use supercell time-dependent DFT (TD-DFT) calculations to correlate observed UV-Vis spectral features with specific Cu motifs. We find that spectra computed for single, static, minimum energy structures are in poor agreement with experimental observation, because Cu ion dynamics have a significant impact on computed spectral features even at ambient temperature. We construct synthetic spectra by averaging over configurations visited during finite-temperature ab initio molecular dynamics (AIMD) simulations and show that these dynamically averaged spectra correspond closely with experimental observation. Further, experimental and simulated spectra are compared to identify features associated with a confounding subset of Cu dimers or larger aggregates in samples prepared to contain predominantly $[CuOH]^+$ species. These results resolve several inconsistencies in spectral and site assignments reported in Cu-exchanged zeolites.

2 Results

2.1 Z_2Cu

First, UV-Vis spectra were collected on a Cu-SSZ-13 sample that contains only Z_2Cu sites.[38,65] This sample was prepared by starting from an SSZ-13 sample (Si/Al = 5) crystallized using a mixture of $TMAda^+$ and Na^+ cations to contain a finite and detectable fraction of paired Al sites,[39] followed by aqueous ion exchange with a cupric nitrate solution to achieve a composition (Cu/Al = 0.21) demonstrated previously to contain only isolated Z_2Cu sites through X-ray absorption spectroscopy, Brønsted acid site exchange stoichiometries with Cu^{2+} and Co^{2+} (2 H^+ replaced per Cu^{2+} or Co^{2+}), and IR spectroscopy[38] (sample preperation details in SI Section S2.1 and elemental analysis in SI Table S4). This Cu-SSZ-13 sample was treated in flowing dry air to 673 K for 2 h, cooled to 300 K, and UV-Vis spectra were collected from 7000 to 50 000 cm^{-1}. Spectra are reported in quasi-absorption (K.M.) units in Figure 1a, and show a broad d-d transition feature from about 8000 to 16 000 cm^{-1} characteristic of a d^9 Cu^{2+} ion and a broad ligand-to-metal charge transfer (LMCT) feature from about 30000 to 50 000 cm^{-1}. The spectrum is consistent with that previously reported for a Cu-SSZ-13 sample after high temperature oxidative treatment.[6]

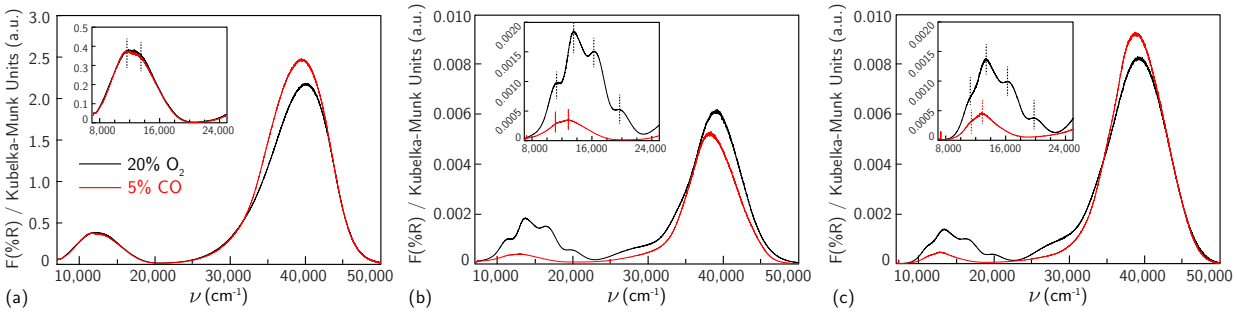

Figure 1: UV-visible spectra collected at 300 K of samples containing predominantly (a) Z_2Cu (Si/Al=5, Cu/Al=0.21), (b) ZCuOH (Si/Al=15, Cu/Al=0.24) and (c) ZCuOH (Si/Al=15, Cu/Al=0.15), after 20% O_2 treatment at 673 K (black), and 5% CO treatment at 523 K (red). Insets show magnification of the d-d transition region.

The Cu^{2+} ions in this zeolite sample are associated with ensembles of two Al centers

separated by two or one intervening Si tetrahedral (T-) sites in the same six-membered ring (6MR), which we term "para" and "meta" respectively. We used a triclinic 12 T-site SSZ-13 supercell described elsewhere[11,66] to represent each ensemble (Figure 2). In each case, a single Cu ion was placed within the 6MR and the structure annealed at 673 K for 150 ps using thermostated AIMD (computational details in SI Section S1). 400 equally spaced configurations were extracted from the trajectories and relaxed. In each Al ensemble, all configurations relaxed to one of three energy minima shown in Figures 2a and 2e. These three minima differ in the combination of Al-adjacent and non-Al-adjacent framework oxygen (O_f) that comprise the first Cu coordination sphere. The framework distorts to accommodate these different Cu-containing minima, behavior consistent with structural distortions reported previously in calculations of metal-exchanged MFI,[67,68] MOR,[67,69] and FER,[70] and inferred from the appearance of two T−O−T deformation bands (900, 950 cm^{-1}) in DRIFTS spectra after Cu exchange into SSZ-13.[71] Despite these structural differences, the three para configurations differ in energy by less than 5 and meta by less than 20 kJ mol^{-1} (Figure 2a, 2e, and also SI Table S1). The lowest-energy para and meta configurations differ in absolute energy by 21 kJ mol^{-1} (SI Table S1).

We performed additional AIMD at 300 K to gain insight into variations in Cu coordination environment at finite temperature[38,72] that might influence the observed spectra. Figure 2b reports histograms of distances between Cu and each of the six 6MR O_f, collected at 0.6 fs intervals over the 150 ps simulation of para Z_2Cu. Distances segregate into two groups centered at 2.1 and 3.3 Å, corresponding to Cu-coordinated and free O_f, each group having widths >0.5 Å (Table S2) that arise from finite temperature fluctuations of the lattice and Cu. The unimodal O1, O2 and O3 and bimodal O4, O5, and O6 distributions are due to transitions between the three different minimum energy configurations of Figure 2a. Inspection of the trajectory shows that transitions occur by extension of the four Cu−O_f bonds, distortion of the lattice, and relaxation into an adjacent minimum. We used these observations to categorize each AIMD frame into one of the three minima or into an inter-

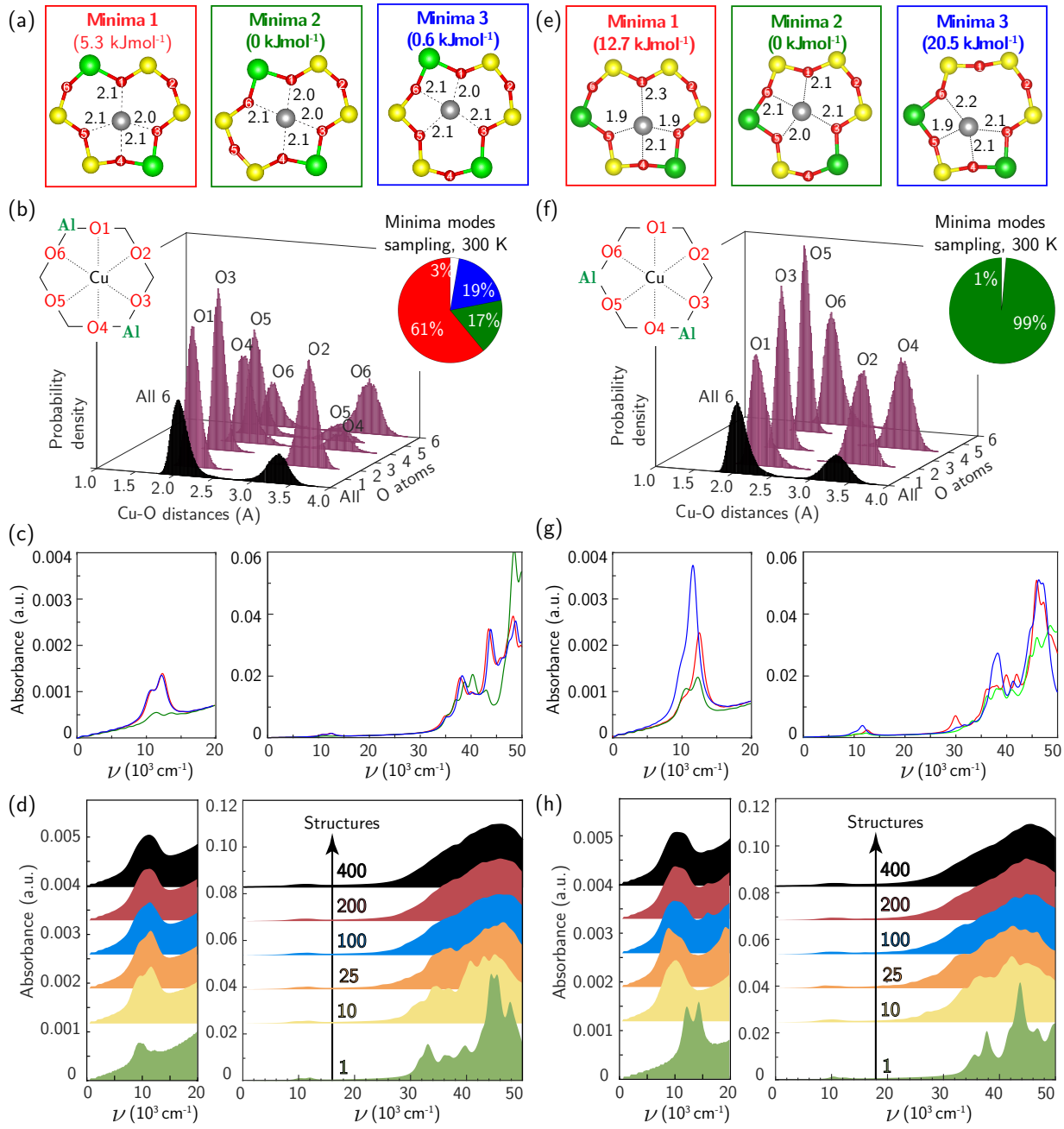

Figure 2: (a) DFT-computed local Cu environment in three Z_2Cu para minima. (b) Individual and aggregate para Z_2Cu Cu$-O_f$ distance histograms collected over 150 ps 300 K AIMD. Inset indicates percent time spent in each minimum. (c) TD-DFT-computed UV-Vis spectra of three Z_2Cu para minima, color-coded by (a). (d) UV-Vis spectra averaged over 1 (green), 10 (yellow), 25 (orange), 100 (blue), 200 (red), and 400 (black) para Z_2Cu snapshots equally spaced in time along the 150 ps trajectory. (e)-(h) Corresponding results for Z_2Cu meta configuration.

mediate state (example structure in SI Figure S2), based on the identity and number of O_f within 2.6 Å of Cu, chosen to represent the upper bound of a Cu−O coordination and shown in the pie chart inset to Figure 2b. All three minima are visited, and the fractions of time spent in each is generally consistent with the relative energies of the corresponding minima. A non-negligible fraction of time is also spent outside any minimum.

Analogous results for meta Z_2Cu are shown in Figure 2f. Again, Cu−O_f distances segregate into the same two groups, and the aggregate histogram of all Cu−O_f distances have identical means and standard deviations in the para and meta cases. The individual Cu−O_f histograms are all unimodal. The large energy difference between minima guarantees that meta Z_2Cu remains in the lowest energy configuration throughout the simulation.

We used TD-DFT to compute frequency-dependent dielectric tensors and corresponding optical absorption spectra of the six minima. The computational details and codes for the VASP inputs and subsequent analysis are provided in SI Section S1.2 and also on the external Zenodo repository (https://doi.org/10.5281/zenodo.1473128). Computed spectra are shown in Figure 2c and 2g, reported in arbitrary K.M. units. All six spectra exhibit features in the d-d and LMCT regions not evident in the experimental spectrum in Figure 1a. Coordinatively similar (as measured from Cu−O distances and O−Cu−O angles) para minima 1 and 3 and meta minimum 2 exhibit equivalent spectra. Absolute intensities are greatest for lowest symmetry and least for highest symmetry minima.[73] Neither any individual spectrum nor a Boltzmann weighting of all spectra at 300 K (shown in SI Figure S3) recovers the experimental spectrum in Figure 1a.

To simulate the effects of these geometric variations on observed spectra, we computed the absorption spectra of 400 equally spaced snapshots from the 300 K AIMD trajectories (SI Figure S4a (para), Figure S4b (meta)). Individual spectra are sensitive to local structure. The d-d transitions shift generally to higher frequency with decreasing mean Cu−O_f distance (SI Figure S5), consistent with behavior expected from ligand field arguments. The LMCT features do not simply correlate with the Cu−O_f distances. Figure 2d and 2h show the

results of averaging increasing numbers of spectra computed from configurations extracted with equal spacing along the AIMD trajectories. Sharp features in both the d-d and LMCT regions become broadened upon averaging an increasing number of spectra from 1 to 200 structures and converge at approximately 200 structures, as evidenced by the small changes resulting from further averaging up to 400 structures. In contrast to spectra computed from the minimum energy structures, the final averaged meta and para UV-Vis spectra are indistinguishable and consistent with experimental observations in Figure 1a.

2.2 ZCuOH

For comparison to the sample containing predominantly Z_2Cu sites, we synthesized different Cu-SSZ-13 samples that contain predominantly the ZCuOH site motif that results when Cu^{2+} ions are exchanged near isolated framework Al sites. We previously reported that crystallization of SSZ-13 zeolites in the presence of only $TMAda^+$ cations produces a material with predominantly isolated framework Al, reflected in the inability to exchange divalent Co^{2+} cations.[39,40] A sample of SSZ-13 (Si/Al = 15) was synthesized using this method and exchanged with differents amounts of Cu^{2+} (Cu/Al = 0.15, 0.24) to generate two Cu-SSZ-13 samples of different ZCuOH density (sample preperation details and elemental analysis in SI Section S2.1 and Table S4).

After Cu^{2+} ion exchange, each model ZCuOH sample was treated in flowing oxygen at 673 K (20% O_2, balance He) for 120 mins (details in SI Section S2.2). UV-Vis spectra of these Cu-SSZ-13 samples collected at 300 K are shown in Figure 1b and 1c. Spectra of both samples show absorbance features in the 8000 to 22 000 cm^{-1} region that are centered around $\sim$ 11059, 13593, 16379, and 20 077 cm^{-1}, and a shoulder in the 24000 to 30 000 cm^{-1} range, and these features are higher in intensity for the sample with higher Cu content. These spectra are similar to those reported following similar pretreatments of Cu-SSZ-13 materials that are expected to contain predominantly ZCuOH species,[18,48,50] by virtue of the Na^+-free synthesis methods used to prepare the parent SSZ-13 sample. In contrast, these spectra are

markedly different from those reported on materials expected to only contain Z_2Cu species (Korhonen et al.[6] and Figure 1a). The four d-d transitions have different relative intensities in the two Cu-SSZ-13 samples shown in Figures 1b and 1c. Literature Cu-SSZ-13 samples prepared to contain ZCuOH sites and exposed to the same O_2 pre-treatment also share the same four d-d transitions but again with different relative intensities.[18,48,50] We conclude that a mononuclear ZCuOH species cannot be solely responsible for the quadruplet feature. The sample-dependent variation suggests the presence of additional multinuclear ZCuOH-derived species with structures and populations that depend on synthesis, treatment and composition.

Da Costa et al.[15] reported that CO reduces multinuclear Cu-oxo species in Cu-ZSM-5 to isolated Cu^+ (d^{10}) ions that do not exhibit d-d transitions. Similarly, we hypothesize that multinuclear Cu-oxo species present in Cu-SSZ-13 samples after treatment in O_2 at 673 K will be reduced by CO at 523 K, leaving behind only isolated ZCuOH species and any residual Z_2Cu sites. Model Z_2Cu and ZCuOH samples were held in a flowing stream of 5% CO at 523 K until no further changes in UV-Vis spectra were observed (details in SI Section S2.4), prior to sealing the UV-Vis cell and cooling to 300 K to record the spectra shown in Figure 1, an approach similar to that applied by Ipek et al. to Cu-SSZ-13 samples containing mixtures of Z_2Cu and ZCuOH sites.[18] As expected, no changes were observed to the d-d transition region in the spectrum of the Z_2Cu sample upon CO exposure (Figure 1a). In sharp contrast, the d-d features at 16379 and 20 077 cm^{-1} and LMCT transition at 27 000 cm^{-1} in the spectra of both ZCuOH samples (Figures 1b and 1c) disappeared after exposure to CO, and features at 11059 and 13 593 cm^{-1} were shifted to 11350 and 13 000 cm^{-1} and decrease markedly in absorbance. Despite differences in the d-d quadruplet feature intensity that are detectable after high temperature O_2 treatment, the d-d transition features of both ZCuOH samples become similar after CO treatment. These findings indicate that not all Cu^{2+} sites in Cu-SSZ-13 are reducible to Cu^+ in the presence of CO, that the Cu^{2+} sites remaining after CO reduction are similar for both samples (Figure 1b and 1c, red), and that these signatures are

of isolated ZCuOH sites.

We used the same triclinic supercell to describe a $[CuOH]^+$ ion-exchanged near an isolated Al. Each T-site in the chabazite lattice is common to two 8MR, one 6MR, and three 4MR. We used 473 K AIMD and geometry optimizations to compare the energies of the $[CuOH]^+$ ion in each of these orientations. The two 8MR orientations are isoenergetic and the Cu-X (X=Si, Al, O) radial distribution function (RDF) computed from their AIMD trajectories are identical (SI Figure S6). From a nudged elastic band calculation, the two 8MR minima are separated by a 63 kJ mol^{-1} barrier (SI Figure S7). Similar calculations with the $[CuOH]^+$ ion directed into a 6MR and 4MR result in configurations 15 and 45 kJ mol^{-1} higher in energy. We thus expect a $[CuOH]^+$ ion to adopt and remain in one of the 8MR orientations at typical conditions of observation here.

Again to explore the consequence of ion dynamics on spectroscopy, we performed additional AIMD simulations at 300 K for 150 ps on a $[CuOH]^+$ ion in one of the 8MR orientations. During the course of the simulation the Cu ion remained coordinated to the same two O_f, bond distances fluctuated, and the OH ligand rotated between Cu-OH rotational conformers twice. Figure 3b reports histograms of the two Cu$-O_f$ and Cu$-$OH distances. The Cu$-$OH bond is shorter and has a narrower distribution than the Cu$-O_f$ bond. The Cu$-O_f$ mean distance are slightly shorter than those from the Z_2Cu simulations while the standard deviations are the same as the Z_2Cu trajectories (SI Table S2). Thus, the coordination environment around ZCuOH varies less than Z_2Cu. The inset to Figure 3b reports the fraction of the trajectory spent in each of the two rotational conformations.

The 8MR $[CuOH]^+$ ion can exist in one of two rotational conformers that differ in energy by 6 kJ mol^{-1} and are distinguished by whether the OH ligand points into or out of the 8MR (Figure 3a). Figure 3c reports the computed UV-Vis spectra of a relaxed 8MR $[CuOH]^+$ ion; each conformer yields a spectrum with two equivalent sharp features in the d-d transition region and a single sharp LMCT band. Predicted ZCuOH absorption intensities are less than either the Z_2Cu para and meta spectra in Figure 2c and 2g, consistent with the higher

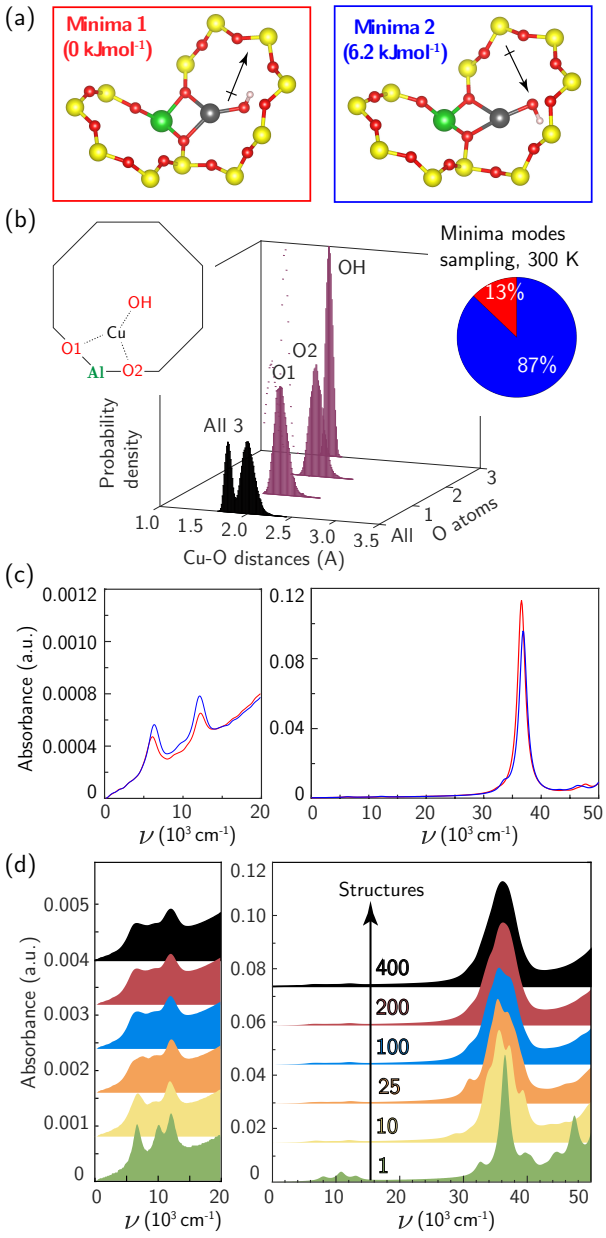

Figure 3: (a) DFT-computed local Cu environment in two 8MR ZCuOH minima. (b) Individual and aggregate Cu−O distance histograms collected over 150 ps of 300 K AIMD. Inset indicates percent time spent in each minimum. (c) TD-DFT-computed UV-Vis spectra of two ZCuOH minima, color-coded by (a). (d) UV-Vis spectra averaged over 1 (green), 10 (yellow), 25 (orange), 100 (blue), 200 (red), and 400 (black) snapshots equally spaced in time along the 150 ps trajectory.

symmetry of ZCuOH and prior predictions that ZCuOH may have small or unobservable d-d transition.[49,74] However the two spectra in Figure 3c for the two ZCuOH isomers are only in rough correspondence with the observed spectrum of the ZCuOH samples.

We computed the absorption spectra of 400 equally spaced structures chosen from the 300 K AIMD simulation; all computed spectra are overlaid in Figure S4c. Significant variations are present in the d-d (7000 to 14 000 cm^{-1}) and LMCT (30000 to 50 000 cm^{-1}) regions (SI Figure S6c), with shorter mean Cu−O distances again correlating with shifts to higher frequency d-d transitions (SI Figure S5). Figure 3d reports spectra averaged over 1, 10, 25, 100, 200, and 400 structures. The two sharp d-d features at 8000 and 13 000 cm^{-1} broaden and begin to merge, while the LMCT region converges to a peak spanning 30000 to 45 000 cm^{-1}. The averaged d-d and LMCT regions ≈1000 cm^{-1} are red-shifted but similar in shape to those observed after CO reduction of the ZCuOH samples (Figure 1b, 1c). Further, the decrease in computed intensity of the d-d relative to LMCT bands in ZCuOH compared to Z_2Cu models corresponds with experimental observation. These observations support both the assignment of the Figure 1b and 1c spectra following CO treatment (red) to isolated ZCuOH and the conclusion that the quadruplet features after O_2 treatment (black) cannot be solely assigned to ZCuOH but rather have contributions from multinuclear Cu complexes.

2.3 Cu Dimers

The additional features in Figure 1b and 1c following 673 K 20% O_2 treatment are from CO-reducible Cu species. A discrete, exchanged $[CuO]^+$ ion is an unlikely candidate because it has a unfavorable computed formation free energy and its computed spectrum (SI Figure S8) is inconsistent with experimental observation. More likely are dimeric or larger Cu clusters. To test the potential for isolated ZCuOH to condense into dimers, we considered two $[CuOH]^+$ ions located at Al separated by four T-sites in the same 8-MR using a 36-T-site supercell. Figure 4a, structures C and E show the $ZCu(OH)_2CuZ$ condensation

product and of its ZCuOCuZ dehydration product, respectively (details in SI Section S1.12 and Figure S9). Within the generalized gradient and harmonic approximations, the free energies to form $ZCu(OH)_2CuZ$ and dehydrate to ZCuOCuZ are computed to be −108 and $-116\,\mathrm{kJ\,mol^{-1}}$, respectively (details in SI Section S1.12). These energetics are consistent with the formation of dimers from $[CuOH]^+$ ions of suitable proximity.

We performed 150 ps AIMD at 300 K on these two dimer structures in the 12-T-site supercell. In both trajectories the dimers remain roughly in the plane of the 8MR and retain coordination to the same bridging and framework O, unlike the more dynamic Z_2Cu behavior described above. Both dimers vibrate internally and against the framework. Histograms of the Cu−O and Cu−Cu distances are shown in Figure 4b and 4c. In ZCuOCuZ, $Cu-O_b$ (bridging O) distances are systematically shorter and fluctuate less than $Cu-O_f$. The Cu−Cu separation oscillates around 2.7 Å, and Cu−O−Cu angle varies from 90 to 115°. The $Cu(OH)_2Cu$ core of $ZCu(OH)_2CuZ$ remains essentially planar and tilted at an angle of ≈35° with respect to the 8MR plane during the AIMD (structure in SI Figure S12). The $Cu-O_b(H)$ and $Cu-O_f$ distances cover a similar range, and the Cu−Cu separation oscillates around 3 Å.

We used TD-DFT and spectral averaging methods identical to those above to simulate UV-Vis spectra of both dimers at 300 K. We observed computed spectra to be sensitive to the geometries of the dimers, similar to the monomer Z_2Cu and ZCuOH. Figure S10 shows spectra averaged over various numbers of snapshots; spectral averaging converge after ≈ 200 structures. Figure 4d shows the spectra averaged over 400 snapshots. The spectrum of $ZCu(OH)_2CuZ$ structure (C) exhibits a broad and low intensity d-d feature around $12\,400\,\mathrm{cm^{-1}}$ and a LMCT band blue-shifted to beyond $50\,000\,\mathrm{cm^{-1}}$. In contrast, the spectrum of ZCuOCuZ structure (E) has two distinct d-d features around 8500 and $12\,400\,\mathrm{cm^{-1}}$ and an LMCT band edge that begins near $30\,000\,\mathrm{cm^{-1}}$. These two are clearly distinct from one another and from the computed spectrum of ZCuOH.

The spectroscopy of Cu dimers may be sensitive to Al proximity, through its influence on geometric and electronic structures. To test this effect, we constructed two additional ZCuOCuZ models with two Al placed third- and second- nearest-neighbor in an 8MR and introduced a Cu−O−Cu dimer so as to maintain Cu−O distances and a Cu−O−Cu angle similar to previous reports.[11,18] Figure 4a shows the optimized structures F and G used to initiate subsequent dynamics. At 3NN, the ZCuOCuZ dimer is symmetrically coordinated to O_f associated with Al; at 2NN, this symmetry is broken, although both Cu remain bound to two O_f. During subsequent 300 K AIMD simulations the Cu ions retain their coordination; as shown in the histograms, Cu−O distances vary across the same ranges at all Al placements while Cu−Cu distances and Cu−O−Cu angles vary considerably with Al separation. While the computed spectra of the optimized structures are different, these differences largely disappear during averaging. As shown in Figure 4d, averaged spectra have similar d-d features and differ only in the LMCT band edge position.

The Cu dimer spectroscopy could also be sensitive to geometric isomerism. To test this effect, we considered several examples of Cu dimers bridged by two O, a well known motif that exhibits several geometric isomers that are sensitive to Al separation.[34,74–76] Figure 4a structures A, B, and D correspond to three different Al placements and three different isomers, all of which were obtained by geometry relaxations beginning from literature structures.[11,18] A and B have triplet and D has a singlet ground states, consistent with earlier results.[34,75] Computed spectra at the optimized geometries (SI Figure S10) exhibit sharp and distinct peaks in both the d-d and LMCT regions. We performed AIMD on all three isomers; distance histograms collected during the simulations are shown in Figure 4b and Figure 4c. The dioxo dimer D is the least variable across the trajectory; dimers A and B sample much larger Cu−O_f and Cu−Cu distances, respectively. During the finite temperature simulation, dimer A moves from a cis to a trans μ-peroxo orientation whereas the optimized geometry has a slightly twisted O−O linkage, resulting in smaller Cu−O−O angles (geometry comparison in SI Figure S13). Figure 4d reports computed spectra averaged over 400 snapshots. Spectra

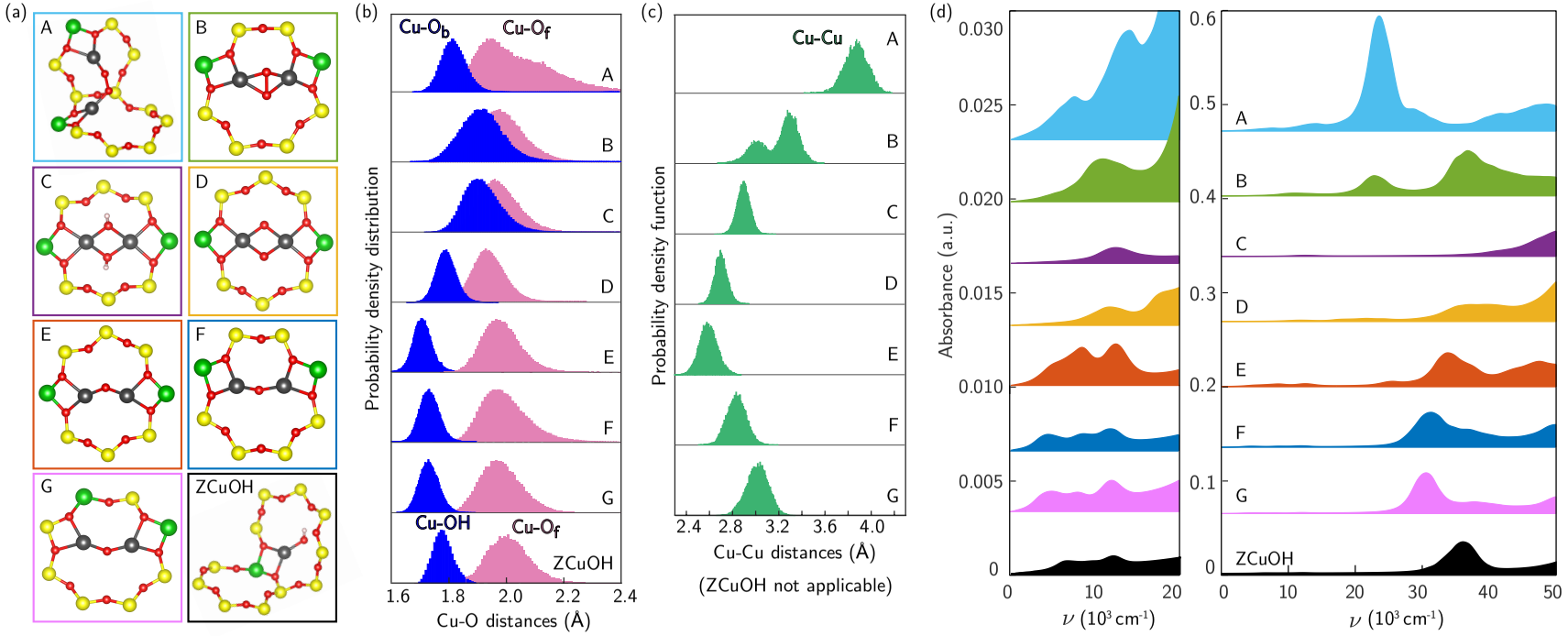

Figure 4: (a) Optimized geometries of Cu dimers A-G, and ZCuOH for reference. (b)/(c) Aggregate Cu-O distance (b) and Cu-Cu distance (c) histograms for dimers A-G and ZCuOH collected over 150 ps 300 K AIMD. Bridging O_b and OH distances are presented in blue, O_f distances are in pink, Cu-Cu distances are in green. (d) Averaged spectra of Cu dimers A-G (left panel is from 0-20000 cm^{-1}, right panel is from 0 to 50000 cm^{-1}, each spectra is offset on the y-axis. Colors of spectra are consistent with those in (a). Averaged ZCuOH spectrum is plotted at the bottom in black for reference.

differ significantly in band location and intensity both in the d-d and LMCT regions.

UV-Vis spectra are thus sensitive to Cu dimer composition and structure and dynamics. Comparisons with the experimental spectra collected after 20% O_2 treatment at 673 K in Figure 1b and c are complicated by the ill-defined number and nuclearity of Cu species present in the samples. Nevertheless, we can make some useful connections. The relative intensities of the d-d transitions for some dimeric Cu species (in particular A, B, and E) are computed to be greater than that of monomeric ZCuOH, consistent with the observation of decreases in d-d peak intensity following CO reduction. Structures B, E, and F have features that roughly correspond with those observed at 11059, 13593, 16379, and 20 077 cm^{-1} (Figure 1b and c), but red-shifted by an amount similar to that found in the comparison of computed and observed ZCuOH spectra. Structures C and D contain features that are plausible candidates for the features observed at 16000 and 19 000 cm^{-1}. Structures A and B contain features that could account for the the broad low energy LMCT shoulder from $\approx$ 22000 to 27 000 cm^{-1} that disappears after the CO reduction treatment. All these results imply that the variations in the quadruplet feature in the d-d region of nominally ZCuOH samples shown in Figures 3b and 3c are associated at least in part with the contributions of different numbers and/or types of dimers from sample to sample.

3 Discussion

Cu-SSZ-13 samples used here and reported in the literature are now well understood to be intrinsically heterogeneous at the microscopic scale, as a result of variations in composition and location of Al[77] and charge-compensating Cu ions, among other factors. Some of these differences are readily observed spectroscopically; for instance ZCuOH sites are clearly indicated by their distinctive O−H stretch vibration at 3660 cm^{-1},[38,78,79] while others are more subtle to infer. The UV-vis results reported here provide some guidance for distinguishing three types of Cu species. Z_2Cu species are distinguished by relatively intense d-d transitions with

maxima near 12 000 and 14 000 cm^{-1} (Figure 1a), and these features persist upon exposure to CO. Isolated ZCuOH species are indicated by lower intensity d-d features near 11 000 and 13 000 cm^{-1} , which also persist during exposure to CO. We find that samples intentionally prepared to contain exclusively ZCuOH always contain a confounding set of species that have relatively intense but irregular d-d features, which we assign to a mixture of higher nuclearity Cu oxo and hydroxo species. These species contribute four relatively prominent features in the d-d region, but they do not persist following CO reduction treatments.

Discrimination within these sets is more challenging. Samples prepared to contain only Z_2Cu species potentially contain two geometrically distinct sites distinguished by the location of the charge-compensating Al,[80] and such sites are predicted here to have distinct UV-Vis spectra if computed at one minimum energy structure. Accounting for the finite temperature fluctuations in Cu location between local minima and associated fluctuations in Cu coordination environment, however, attenuates these differences, such that the two sites become spectroscopically indistinguishable. Similar factors affect the interpretation of XAS[79,81–84] , EPR[49,83,85] spectroscopies, and X-ray diffraction[5,82,85,86] patterns, and caution should be applied in inferring Z_2Cu geometric information by comparison of observations to predictions from single, minimum energy structures.

In samples in which Cu exchange is predominantly associated with isolated Al T-sites and contain a majority of ZCuOH sites, observed UV-Vis spectra contain features in the d-d and LMCT regions that cannot be accounted for by the spectrum computed of these sites.[18,48,49,87] Strategies to directly prepare and characterize Cu-SSZ-13 samples that contain exclusively ZCuOH sites, either by exchanging dilute amounts of Cu or using higher silica-content SSZ-13 supports, are unlikely to be successful because of the difficulties of observing dilute ZCuOH and the presence of a confounding set of framework Al sites that can stabilize dimeric forms of Cu even at low Al density. Therefore, a strategy that combines synthetic efforts to bias formation of predominantly one Cu site type with treatments that selectively remove minority Cu species, is more likely to allow access to individual Cu site types.

The exact shapes and positions of the features depend on the zeolite composition and the precise pretreatment conditions, including temperature, pressure and duration of O_2 exposure, all suggestive of additional Cu sites produced dynamically. Calculations here show that [$CuOH^+$] ions can move between adjacent 8MRs with an activation barrier of 63 kJ mol^{-1} (SI Figure S7) and that suitably proximal ions can condense into dimers. This proposal is consistent with experimental observations of a decrease in the approximately 3660 cm^{-1} vibrational feature associated with the ZCuO−H stretch with increasing temperature,[41] corresponding Raman shifts for multiple Cu_2O_x motifs.[18,19,55] It is also consistent with the observation of dry NO oxidation to NO_2 on nominally ZCuOH-containing samples, ascribed to dimeric Cu sites.[11,88] Because computed UV-Vis spectra of Cu dimers (Figure 4) are sensitive to Al proximity, extra-lattice ligands, and to finite temperature structural fluctuations, assignment of specific spectroscopic features to individual types of dimeric Cu species is not possible based on results reported here. .

The samples prepared to contain Z_2Cu sites have spectral features that are invariant to reduction in CO. Literature results on similar samples find that they are insensitive to exposure to He, O_2, or CH_4.[6,19] The four features observed in the d-d region of the ZCuOH samples following oxidizing treatment are similar to those reported previously in similar samples,[18,48,50] but these bands do respond differently to subsequent reducing treatments. We find that 5% CO exposure at 523 K reproducibly preserves a portion of the d-d and LMCT features, which we assign to isolated ZCuOH sites. In contrast, exposure to CH_4 at 473 K results only in a decrease in the lower energy portion (25000 to 38 000 cm^{-1}) of the LMCT band and disappearance of the 29 000 cm^{-1} band.[18,50,87] These results suggest that at the same temperature CH_4 reduces a different population of $Cu_xO_yH_z$ moieties to Cu^+ than exposure to inert (He), and exposure to CO reduces all of the $Cu_xO_yH_z$ observed to reduce in either CH_4 or He.[18] Spectral features we assign here to isolated ZCuOH moieties are observed in similar materials to persist after CH_4 exposure.[18,50] Precise identification of the Cu dimer sites responsible for CH_4 activation under different conditions remains an

important challenge for experiment and computation.

4 Conclusions

Cu-exchanged zeolites remain a topic of great scientific interest because of their intriguing performance in catalyzing difficult transformations involving the nitrogen oxides and methane. Identification of active sites is complicated by the sensitivity of Cu exchange to zeolite framework types, the number and distribution of framework Al atoms, Cu content, and pretreatment conditions. The SSZ-13 zeolite framework is constructed of a single symmetry-distinct type of T-site, in principle reducing the number of possible distinct ion exchange sites and thus simplifying spectroscopic interrogation of those sites. Here we use directed synthetic approaches to emphasize different types of exchange sites, and DFT evaluations of site structure and spectral signatures to test this principle. We find that in SSZ-13 samples prepared to contain only isolated Al T-sites, and thus in principle a homogeneous array of $[CuOH]^+$ ion exchange sites, always contain a confounding subset of O- or OH-bridged Cu dimers and/or larger aggregates in the Cu/Al exchange regime explored here. These latter species are intrinsically heterogeneous due to heterogeneity in bridging ligands and/or in arrangements of framework Al substituents, which likely involve more than one Al T-site. The underlying $[CuOH]^+$ UV-Vis spectrum can be revealed by selective CO reduction of the polynuclear Cu species. The UV-Vis spectrum, even of isolated $[CuOH]^+$ ions, is found to be influenced by the intrinsic, finite-temperature dynamics of the site, as revealed through AIMD and TD-DFT calculations. In SSZ-13 samples prepared to contain 2NN (meta) and 3NN (para) Al pairs in the 6MR, the same dynamical factors serve to obscure spectroscopic differences between these two distinct types of Z_2Cu sites. While calculations performed at the optimized geometries predict that the meta and para Cu-exchange sites are spectroscopically distinct, those differences are indistinguishable after accounting for the finite-temperature fluctuations in Cu ion coordination environment.

These results highlight the potential and the practical challenges of developing correlations between observed spectroscopy and the contributions of various Cu ion exchange sites and motifs to observed chemical reactivity. They highlight that precise characterization of active sites in this and similar systems demands a careful integration of chemical and spectroscopic interrogation with computational models that account for the structural and dynamical complexities of the materials.

Acknowledgement

The experimental research at Purdue on zeolite synthesis and characterization was supported by the U.S. Department of Energy, Office of Science, Office of Basic Energy Sciences, under Award Number DE-SC0019026. The computational work at Notre Dame was supported by the National Science Foundation GOALI program under award number CBET-1258690. We thank the Center for Research Computing at Notre Dame, and EMSL, a DOE Office of Science User Facility sponsored by the Office of Biological and Environmental Research and located at Pacific Northwest National Laboratory, for support of computational resources. We thank John R. Di Iorio (Purdue) for assistance with zeolite synthesis and helpful technical discussions. Florian Göeltl contributions were supported in part through NSF grant number CHE-1800284.

Supporting Information Available

The following files are available free of charge.

- cussz13-uvvis-supplemental.pdf

This material is available free of charge via the Internet at `http://pubs.acs.org/`.

References

(1) Paolucci, C.; Di Iorio, J.; Ribeiro, F.; Gounder, R.; Schneider, W. *Adv. Catal.*; Elsevier, 2016; Vol. 59; pp 1–107.

(2) Beale, A. M.; Gao, F.; Lezcano-Gonzalez, I.; Peden, C. H.; Szanyi, J. Recent advances in automotive catalysis for NOx emission control by small-pore microporous materials. *Chem. Soc. Rev.* **2015**, *44*, 7371–7405.

(3) Gao, F.; Kwak, J. H.; Szanyi, J.; Peden, C. H. Current understanding of Cu-exchanged chabazite molecular sieves for use as commercial diesel engine DeNOx catalysts. *Top. Catal.* **2013**, *56*, 1441–1459.

(4) Nova, I.; Tronconi, E. *Urea-SCR technology for deNOx after treatment of diesel exhausts*; Springer, 2014.

(5) Fickel, D. W.; Lobo, R. F. Copper coordination in Cu-SSZ-13 and Cu-SSZ-16 investigated by variable-temperature XRD. *J. Phys. Chem. C* **2010**, *114*, 1633–1640.

(6) Korhonen, S. T.; Fickel, D. W.; Lobo, R. F.; Weckhuysen, B. M.; Beale, A. M. Isolated Cu^{2+} ions: active sites for selective catalytic reduction of NO. *Chem. Commun.* **2011**, *47*, 800–802.

(7) Marberger, A.; Petrov, A. W.; Steiger, P.; Elsener, M.; Kröcher, O.; Nachtegaal, M.; Ferri, D. Time-resolved copper speciation during selective catalytic reduction of NO on Cu-SSZ-13. *Nat. Catal.* **2018**, *1*, 221–227.

(8) Janssens, T. V.; Falsig, H.; Lundegaard, L. F.; Vennestrøm, P. N.; Rasmussen, S. B.; Moses, P. G.; Giordanino, F.; Borfecchia, E.; Lomachenko, K. A.; Lamberti, C. A consistent reaction scheme for the selective catalytic reduction of nitrogen oxides with ammonia. *ACS Catalysis* **2015**, *5*, 2832–2845.

(9) Lomachenko, K. A.; Borfecchia, E.; Negri, C.; Berlier, G.; Lamberti, C.; Beato, P.; Falsig, H.; Bordiga, S. The Cu-CHA deNO x Catalyst in Action: Temperature-Dependent NH3-Assisted Selective Catalytic Reduction Monitored by Operando XAS and XES. *Journal of the American Chemical Society* **2016**, *138*, 12025–12028.

(10) Kwak, J. H.; Tonkyn, R. G.; Kim, D. H.; Szanyi, J.; Peden, C. H. Excellent activity and selectivity of Cu-SSZ-13 in the selective catalytic reduction of NOx with NH3. *Journal of Catalysis* **2010**, *275*, 187–190.

(11) Verma, A. A.; Bates, S. A.; Anggara, T.; Paolucci, C.; Parekh, A. A.; Kamasamudram, K.; Yezerets, A.; Miller, J. T.; Delgass, W. N.; Schneider, W. F.; Ribeiro, F. H. NO oxidation: A probe reaction on Cu-SSZ-13. *J. Catal.* **2014**, *312*, 179–190.

(12) Ruggeri, M. P.; Nova, I.; Tronconi, E.; Pihl, J. A.; Toops, T. J.; Partridge, W. P. In-situ DRIFTS measurements for the mechanistic study of NO oxidation over a commercial Cu-CHA catalyst. *Appl. Catal. B: Environ.* **2015**, *166*, 181–192.

(13) Centi, G.; Perathoner, S. Nature of active species in copper-based catalysts and their chemistry of transformation of nitrogen oxides. *Appl. Catal. A, General* **1995**, *132*, 179–259.

(14) Groothaert, M. H.; Van Bokhoven, J. A.; Battiston, A. A.; Weckhuysen, B. M.; Schoonheydt, R. A. Bis(μ-oxo)dicopper in Cu-ZSM-5 and its role in the decomposition of NO: A combined in situ XAFS, UV-vis-near-IR, and kinetic study. *J. Am. Chem. Soc.* **2003**, *125*, 7629–7640.

(15) Da Costa, P.; Moden, B.; Meitzner, G. D.; Lee, D. K.; Iglesia, E. Spectroscopic and chemical characterization of active and inactive Cu species in NO decomposition catalysts based on Cu-ZSM5. *Phys. Chem. Chem. Phys.* **2002**, *4*, 4590–4601.

(16) Vanelderen, P.; Vancauwenbergh, J.; Sels, B. F.; Schoonheydt, R. A. Coordination chemistry and reactivity of copper in zeolites. *Coord. Chem. Rev.* **2013**, *257*, 483–494.

(17) Wulfers, M. J.; Lobo, R. F.; Ipek, B.; Teketel, S. Conversion of Methane to Methanol on Copper-Containing Small-Pore Zeolites and Zeotypes. *Chem. Commun.* **2015**, *51*, 4447–4450.

(18) Ipek, B.; Wulfers, M. J.; Kim, H.; Göltl, F.; Hermans, I.; Smith, J. P.; Booksh, K. S.; Brown, C. M.; Lobo, R. F. Formation of $[Cu_2O_2]^{2+}$ and $[Cu_2O]^{2+}$ toward C-H Bond Activation in Cu-SSZ-13 and Cu-SSZ-39. *ACS Catal.* **2017**, *7*, 4291–4303.

(19) Pappas, D. K. et al. Methane to Methanol: Structure-Activity Relationships for Cu-CHA. *J. Am. Chem. Soc.* **2017**, *139*, 14961–14975.

(20) Kulkarni, A. R.; Zhao, Z.; Siahrostami, S.; Nørskov, J. K.; Studt, F. Cation-Exchanged Zeolites for the Selective Oxidation of Methane to Methanol. *Catal. Sci. Technol.* **2017**, *8*, 114–123.

(21) Tomkins, P.; Mansouri, A.; Bozbag, S. E.; Krumeich, F.; Park, M. B.; Alayon, E. M. C.; Ranocchiari, M.; van Bokhoven, J. A. Isothermal Cyclic Conversion of Methane into Methanol over Copper-Exchanged Zeolite at Low Temperature. *Angew. Chem. Int. Ed.* **2016**, *55*, 5467–5471.

(22) Woertink, J. S.; Smeets, P. J.; Groothaert, M. H.; Vance, M. A.; Sels, B. F.; Schoonheydt, R. A.; Solomon, E. I. A $[Cu_2O]^{2+}$ core in Cu-ZSM-5, the active site in the oxidation of methane to methanol. *Proc. Natl. Acad. Sci.* **2009**, *106*, 18908–18913.

(23) Grundner, S.; Markovits, M. A. C.; Li, G.; Tromp, M.; Pidko, E. A.; Hensen, E. J. M.; Jentys, A.; Sanchez-Sanchez, M.; Lercher, J. A. Single-site trinuclear copper oxygen clusters in mordenite for selective conversion of methane to methanol. *Nat. Commun.* **2015**, *6*, 7546.

(24) Borfecchia, E.; Beato, P.; Svelle, S.; Olsbye, U.; Lamberti, C.; Bordiga, S. Cu-CHA–a model system for applied selective redox catalysis. *Chem. Soc. Rev.* **2018**, in press.

(25) Dusselier, M.; Davis, M. E. Small-Pore Zeolites: Synthesis and Catalysis. *Chem. Rev.* **2018**, *118*, 5265–5329.

(26) Snyder, B. E.; Bols, M. L.; Schoonheydt, R. A.; Sels, B. F.; Solomon, E. I. Iron and Copper Active Sites in Zeolites and Their Correlation to Metalloenzymes. *Chem. Rev.* **2017**, *118*, 2718–2768.

(27) Dinh, K. T.; Sullivan, M. M.; Serna, P.; Meyer, R. J.; Dincă, M.; Román-Leshkov, Y. Viewpoint on the Partial Oxidation of Methane to Methanol Using Cu-and Fe-Exchanged Zeolites. *ACS Catal.* **2018**, *8*, 8306–8313.

(28) Latimer, A. A.; Kulkarni, A. R.; Aljama, H.; Montoya, J. H.; Yoo, J. S.; Tsai, C.; Abild-Pedersen, F.; Studt, F.; Nørskov, J. K. Understanding trends in C–H bond activation in heterogeneous catalysis. *Nature materials* **2017**, *16*, 225.

(29) Kulkarni, A. R.; Zhao, Z.-J.; Siahrostami, S.; Nørskov, J. K.; Studt, F. Monocopper active site for partial methane oxidation in Cu-exchanged 8MR zeolites. *ACS Catalysis* **2016**, *6*, 6531–6536.

(30) Pappas, D. K. et al. The nuclearity of the active site for methane to methanol conversion in Cu-mordenite: a quantitative assessment. *J. Am. Chem. Soc.* **2018**, Just Accepted Manuscript.

(31) Sushkevich, V. L.; Palagin, D.; Ranocchiari, M.; van Bokhoven, J. A. Selective anaerobic oxidation of methane enables direct synthesis of methanol. *Science* **2017**, *356*, 523–527.

(32) Li, G.; Vassilev, P.; Sanchez-Sanchez, M.; Lercher, J. A.; Hensen, E. J.; Pidko, E. A. Stability and reactivity of copper oxo-clusters in ZSM-5 zeolite for selective methane oxidation to methanol. *Journal of Catalysis* **2016**, *338*, 305–312.

(33) Lan, Z.; Sharada, S. M. Computational strategies to probe CH activation in dioxo-dicopper complexes. *Phys. Chem. Chem. Phys* **2018**, *20*, 25602–25614.

(34) Goodman, B. R.; Schneider, W. F.; Hass, K. C.; Adams, J. B. Theoretical analysis of oxygen-bridged Cu pairs in Cu-exchanged zeolites. *Catal. Lett.* **1998**, *56*, 183–188.

(35) Trout, B. L.; Chakraborty, A. K.; Bell, A. T. Local spin density functional theory study of copper ion-exchanged ZSM-5. *J. Phys. Chem.* **1996**, *100*, 4173–4179.

(36) Deka, U.; Lezcano-Gonzalez, I.; Weckhuysen, B. M.; Beale, A. M. Local environment and nature of Cu active sites in zeolite-based catalysts for the selective catalytic reduction of NO_x. *ACS Catal.* **2013**, *3*, 413–427.

(37) Dědeček, J.; Sobalík, Z.; Wichterlová, B. Siting and distribution of framework aluminium atoms in silicon-rich zeolites and impact on catalysis. *Catal. Rev.* **2012**, *54*, 135–223.

(38) Paolucci, C.; Parekh, A. A.; Khurana, I.; Di Iorio, J. R.; Li, H.; Albarracin Caballero, J. D.; Shih, A. J.; Anggara, T.; Delgass, W. N.; Miller, J. T.; Ribeiro, F. H.; Gounder, R.; Schneider, W. F. Catalysis in a cage: Condition-Dependent Speciation and Dynamics of Exchanged Cu Cations in SSZ-13 Zeolites. *J. Am. Chem. Soc.* **2016**, *138*, 6028–6048.

(39) Di Iorio, J. R.; Gounder, R. Controlling the Isolation and Pairing of Aluminum in Chabazite Zeolites Using Mixtures of Organic and Inorganic Structure-Directing Agents. *Chem. Mater.* **2016**, *28*, 2236–2247.

(40) Di Iorio, J. R.; Nimlos, C. T.; Gounder, R. Introducing catalytic diversity into single-site chabazite zeolites of fixed composition via synthetic control of active site proximity. *ACS Catal.* **2017**, *7*, 6663–6674.

(41) Borfecchia, E.; Lomachenko, K. A.; Giordanino, F.; Falsig, H.; Beato, P.; Soldatov, A. V.; Bordiga, S.; Lamberti, C. Revisiting the nature of Cu sites in the activated Cu-SSZ-13 catalyst for SCR reaction. *Chem. Sci.* **2014**, *8*, 548–563.

(42) Albarracin-Caballero, J. D.; Khurana, I.; Di Iorio, J. R.; Shih, A. J.; Schmidt, J. E.; Dusselier, M.; Davis, M. E.; Yezerets, A.; Miller, J. T.; Ribeiro, F. H.; Gounder, R. Structural and kinetic changes to small-pore Cu-zeolites after hydrothermal aging treatments and selective catalytic reduction of NO_x with ammonia. *React. Chem. Eng.* **2017**, *2*, 168–179.

(43) Schmidt, J. E.; Oord, R.; Guo, W.; Poplawsky, J. D.; Weckhuysen, B. M. Nanoscale tomography reveals the deactivation of automotive copper-exchanged zeolite catalysts. *Nat. Commun.* **2017**, *8*, 1666.

(44) Göltl, F.; Sautet, P.; Hermans, I. The impact of finite temperature on the coordination of Cu cations in the zeolite SSZ-13. *Catal. Today* **2016**, *267*, 41–46.

(45) Chen, P.; Khetan, A.; Jabłońska, M.; Simböck, J.; Muhler, M.; Palkovits, R.; Pitsch, H.; Simon, U. Local dynamics of copper active sites in zeolite catalysts for selective catalytic reduction of NOx with NH3. *Appl. Catal. B: Environmental* **2018**, *237*, 263–272.

(46) Li, H.; Paolucci, C.; Schneider, W. F. Zeolite Adsorption Free Energies from ab Initio Potentials of Mean Force. *J. Chem. Theory Comput.* **2018**, *14*, 929–938.

(47) Chen, L.; Falsig, H.; Janssens, T. V.; Jansson, J.; Skoglundh, M.; Grönbeck, H. Effect of Al-distribution on oxygen activation over Cu–CHA. *Catal. Sci. Technol.* **2018**, *8*, 2131–2136.

(48) Giordanino, F.; Vennestrøm, P. N. R.; Lundegaard, L. F.; Stappen, F. N.; Mossin, S.; Beato, P.; Bordiga, S.; Lamberti, C. Characterization of Cu-exchanged SSZ-13: a comparative FTIR, UV-Vis, and EPR study with Cu-ZSM-5 and Cu-β with similar Si/Al and Cu/Al ratios. *Dalton Trans.* **2013**, *42*, 12741–61.

(49) Godiksen, A.; Stappen, F. N.; R Vennestrøm, P. N.; Giordanino, F.; Birk Rasmussen, S.; Lundegaard, L. F.; Mossin, S. Coordination Environment of Copper Sites in Cu-CHA

Zeolite Investigated by Electron Paramagnetic Resonance. *J. Phys. Chem. C* **2014**, *118*, 23126–23138.

(50) Oord, R.; Schmidt, J. E.; Weckhuysen, B. M. Methane-to-methanol conversion over zeolite Cu-SSZ-13, and its comparison with the selective catalytic reduction of NO_x with NH_3. *Catal. Sci. Technol.* **2018**, *8*, 1028–1038.

(51) Lei, G. D.; Adelman, B. J.; Sárkány, J.; Sachtler, W. M. H. Identification of copper(II) and copper(I) and their interconversion in Cu/ZSM-5 De-NOx catalysts. *Appl. Catal. B, Environ.* **1995**, *5*, 245–256.

(52) Modén, B.; Da Costa, P.; Fonfé, B.; Lee, D. K.; Iglesia, E. Kinetics and Mechanism of Steady-State Catalytic NO Decomposition Reactions on Cu-ZSM5. *J. Catal.* **2002**, *209*, 75–86.

(53) Modén, B.; Da Costa, P.; Lee, D. K.; Iglesia, E. Transient studies of oxygen removal pathways and catalytic redox cycles during NO decomposition on Cu-ZSM5. *J. Phys. Chem. B* **2002**, *106*, 9633–9641.

(54) Smeets, P. J.; Hadt, R. G.; Woertink, J. S.; Vanelderen, P.; Schoonheydt, R. A.; Sels, B. F.; Solomon, E. I. Oxygen precursor to the reactive intermediate in methanol synthesis by Cu-ZSM-5. *J. Am. Chem. Soc.* **2010**, *132*, 14736–14738.

(55) Woertink, J. S.; Smeets, P. J.; Groothaert, M. H.; Vance, M. A.; Sels, B. F.; Schoonheydt, R. A.; Solomon, E. I. A $[Cu_2O]^{2+}$ Core in Cu-ZSM-5, the Active Site in the Oxidation of Methane to Methanol. *Proc. Natl. Acad. Sci.* **2009**, *106*, 18908–18913.

(56) Groothaert, M. H.; Smeets, P. J.; Sels, B. F.; Jacobs, P. A.; Schoonheydt, R. A. Selective oxidation of methane by the bis(μ-oxo)dicopper core stabilized on ZSM-5 and mordenite zeolites. *J. Am. Chem. Soc.* **2005**, *127*, 1394–1395.

(57) Grundner, S.; Markovits, M. A.; Li, G.; Tromp, M.; Pidko, E. A.; Hensen, E. J.; Jentys, A.; Sanchez-Sanchez, M.; Lercher, J. A. Single-site trinuclear copper oxygen clusters in mordenite for selective conversion of methane to methanol. *Nat. Commun.* **2015**, *6*, 7546.

(58) Sushkevich, V. L.; Palagin, D.; van Bokhoven, J. A. Effect of Active Sites Structure on Activity of Copper Mordenite in Aerobic and Anaerobic Conversion of Methane to Methanol. *Angew. Chem. Int. Ed.* **2018**, *57*, 8906–8910.

(59) van Bokhoven, J. A.; Lamberti, C. In *XAFS Techniques for Catalysts, Nanomaterials, and Surfaces*; Iwasawa, Y., Asakura, K., Tada, M., Eds.; Springer International Publishing: Cham, 2017; pp 299–316.

(60) Kosinov, N.; Liu, C.; Hensen, E. J.; Pidko, E. A. Engineering of transition metal catalysts confined in zeolites. *Chem. Mater.* **2018**, *30*, 3177–3198.

(61) Palagin, D.; Knorpp, A. J.; Pinar, A. B.; Ranocchiari, M.; van Bokhoven, J. A. Assessing the relative stability of copper oxide clusters as active sites of a CuMOR zeolite for methane to methanol conversion: size matters? *Nanoscale* **2017**, *9*, 1144–1153.

(62) Borfecchia, E.; Pappas, D. K.; Dyballa, M.; Lomachenko, K. A.; Negri, C.; Signorile, M.; Berlier, G. Evolution of active sites during selective oxidation of methane to methanol over Cu-CHA and Cu-MOR zeolites as monitored by operando XAS. *Catal. Today* **2018**, in press.

(63) Henson, M. J.; Vance, M. a.; Zhang, C. X.; Liang, H.-C.; Karlin, K. D.; Solomon, E. I. Resonance raman investigation of equatorial ligand donor effects on the $Cu_2O_2^{2+}$ core in end-on and side-on μ-peroxo-dicopper(II) and bis-μ-oxo-dicopper(III) complexes. *J. Am. Chem. Soc.* **2003**, *125*, 5186–5192.

(64) Vanelderen, P.; Hadt, R. G.; Smeets, P. J.; Solomon, E. I.; Schoonheydt, R. A.;

Sels, B. F. Cu-ZSM-5: A biomimetic inorganic model for methane oxidation. *J. Catal.* **2011**, *284*, 157–164.

(65) Paolucci, C.; Khurana, I.; Parekh, A. A.; Li, S.; Shih, A. J.; Li, H.; Iorio, J. R. D.; Albarracin-caballero, J. D.; Yezerets, A.; Miller, J. T.; Delgass, W. N.; Ribeiro, F. H.; Schneider, W. F.; Gounder, R. Dynamic multinuclear sites formed by mobilized copper ions in NOx selective catalytic reduction. *Science* **2017**, *357*, 898–903.

(66) McEwen, J. S.; Anggara, T.; Schneider, W. F.; Kispersky, V. F.; Miller, J. T.; Delgass, W. N.; Ribeiro, F. H. Integrated operando X-ray absorption and DFT characterization of Cu-SSZ-13 exchange sites during the selective catalytic reduction of NOx with NH3. *Catal. Today* **2012**, *184*, 129–144.

(67) Smeets, P. J.; Woertink, J. S.; Sels, B. F.; Solomon, E. I.; Schoonheydt, R. A. Transition-metal ions in zeolites: Coordination and activation of oxygen. *Inorg. Chem.* **2010**, *49*, 3573–3583.

(68) Godiksen, A.; Vennestrøm, P. N. R.; Rasmussen, S. B.; Mossin, S. Identification and quantification of copper sites in zeolites by electron paramagnetic resonance spectroscopy. *Top. Catal.* **2017**, *60*, 13–29.

(69) Snyder, B. E. R.; Bols, M. L.; Schoonheydt, R. A.; Sels, B. F.; Solomon, E. I. Iron and Copper Active Sites in Zeolites and Their Correlation to Metalloenzymes. *Chem. Rev.* **2018**, *118*, 2718–2768.

(70) Sklenak, S.; Andrikopoulos, P. C.; Whittleton, S. R.; Jirglova, H.; Sazama, P.; Benco, L.; Bucko, T.; Hafner, J.; Sobalik, Z. Effect of the Al siting on the structure of Co(II) and Cu(II) cationic sites in ferrierite. A periodic DFT molecular dynamics and FTIR study. *J. Phys. Chem. C* **2013**, *117*, 3958–3968.

(71) Luo, J.; Wang, D.; Kumar, A.; Li, J.; Kamasamudram, K.; Currier, N.; Yezerets, A.

Identification of two types of Cu sites in Cu/SSZ-13 and their unique responses to hydrothermal aging and sulfur poisoning. *Catal. Today* **2016**, *267*, 3–9.

(72) Goeltl, F.; Muller, P.; Uchupalanun, P.; Sautet, P.; Hermans, I. Developing a Descriptor-Based Approach for CO and NO Adsorption Strength to Transition Metal Sites in Zeolites. *Chemistry of Materials* **2017**, *29*, 6434–6444.

(73) Harris, D.; Bertolucci, M. *Symmetry and Spectroscopy: An Introduction to Vibrational and Electronic Spectroscopy*; Dover Books on Chemistry Series; Dover Publications, 1989.

(74) Solomon, E. I.; Heppner, D. E.; Johnston, E. M.; Ginsbach, J. W.; Cirera, J.; Qayyum, M.; Kieber-Emmons, M. T.; Kjaergaard, C. H.; Hadt, R. G.; Tian, L. Copper active sites in biology. *Chem. Rev.* **2014**, *114*, 3659–3853.

(75) Goodman, B. R.; Hass, K. C.; Schneider, W. F.; Adams, J. B. Cluster Model Studies of Oxygen-Bridged Cu Pairs in Cu-ZSM-5 Catalysts. *J. Phys. Chem. B* **1999**, *103*, 10452–10460.

(76) Mahyuddin, M. H.; Tanaka, T.; Shiota, Y.; Staykov, A.; Yoshizawa, K. Methane Partial Oxidation over $[Cu_2(\mu{-}O)]^{2+}$ and $[Cu_3(\mu{-}O)_3]^{2+}$ Active Species in Large-Pore Zeolites. *ACS Catal.* **2018**, *8*, 1500–1509.

(77) Knott, B. C.; Nimlos, C. T.; Robichaud, D. J.; Nimlos, M. R.; Kim, S.; Gounder, R. Consideration of the Aluminum Distribution in Zeolites in Theoretical and Experimental Catalysis Research. *ACS Catal.* **2018**, *8*, 770–784.

(78) Lezcano-Gonzalez, I.; Deka, U.; Arstad, B.; Van Yperen-De Deyne, A.; Hemelsoet, K.; Waroquier, M.; Van Speybroeck, V.; Weckhuysen, B. M.; Beale, A. M. Determining the storage, availability and reactivity of NH3 within Cu-Chabazite-based Ammonia Selective Catalytic Reduction systems. *Phys. Chem. Chem. Phys.* **2014**, *16*, 1639–1650.

(79) Giordanino, F.; Borfecchia, E.; Lomachenko, K. A.; Lazzarini, A.; Agostini, G.; Gallo, E.; Soldatov, A. V.; Beato, P.; Bordiga, S.; Lamberti, C. Interaction of NH3 with Cu-SSZ-13 catalyst: A complementary FTIR, XANES, and XES study. *J. Phys. Chem. Lett.* **2014**, *5*, 1552–1559.

(80) Li, S.; Li, H.; Gounder, R.; Debellis, A.; Müller, I. B.; Prasad, S.; Moini, A.; Schneider, W. F. First-Principles Comparison of Proton and Divalent Copper Cation Exchange Energy Landscapes in SSZ-13 Zeolite. *J. Phys. Chem. C* **2018**, *122*, 23564–23573.

(81) Martini, A.; Borfecchia, E.; Lomachenko, K. A.; Pankin, I.; Negri, C.; Berlier, G.; Beato, P.; Falsig, H.; Bordiga, S.; Lamberti, C.; Pankin, I. A. Composition-driven Cu-speciation and reducibility in Cu-CHA zeolite catalysts: a multivariate XAS/FTIR approach to complexity. *Chem. Sci.* **2017**, *8*, 6836–6851.

(82) Andersen, C. W.; Borfecchia, E.; Bremholm, M.; Jørgensen, M. R. V.; Vennestrøm, P. N. R.; Lamberti, C.; Lundegaard, L. F.; Iversen, B. B. Redox-Driven Migration of Copper Ions in the Cu-CHA Zeolite as Shown by the In Situ PXRD/XANES Technique. *Angew. Chem. Int. Ed.* **2017**, *56*, 10367–10372.

(83) Berlier, G.; Crocellà, V.; Signorile, M.; Borfecchia, E.; Bonino, F.; Bordiga, S. In *Struct. Bond.*; Mingos, M. P. F., Ed.; Springer, Berlin, Heidelberg, 2018; Chapter 1, pp 1–64.

(84) Martini, A.; Alladio, E.; Borfecchia, E. Determining Cu–Speciation in the Cu–CHA Zeolite Catalyst: The Potential of Multivariate Curve Resolution Analysis of In Situ XAS Data. *Top. Catal.* **2018**, *61*, 1396–1407.

(85) Godiksen, A.; Isaksen, O. L.; Rasmussen, S. B.; Vennestrøm, P. N.; Mossin, S. Site-Specific Reactivity of Copper Chabazite Zeolites with Nitric Oxide, Ammonia, and Oxygen. *ChemCatChem* **2018**, *10*, 366–370.

(86) Andersen, C. W.; Bremholm, M.; Vennestrom, P. N. R.; Blichfeld, A. B.; Lundegaard, L. F.; Iversen, B. B. Location of Cu^{2+} in CHA zeolite investigated by X-ray diffraction using the Rietveld/maximum entropy method. *IUCrJ* **2014**, *1*, 382–386.

(87) Oord, R. Spectroscopic Insights into Copper-Based Microporous Zeolites for NH3-SCR of NOx and Methane-to-Methanol Activation. Ph.D. thesis, Utrecht University, 2017.

(88) Gao, F.; Washton, N. M.; Wang, Y.; Kollár, M.; Szanyi, J.; Peden, C. H. Effects of Si/Al ratio on Cu/SSZ-13 NH 3-SCR catalysts: Implications for the active Cu species and the roles of Brønsted acidity. *Journal of Catalysis* **2015**, *331*, 25–38.

Graphical TOC Entry

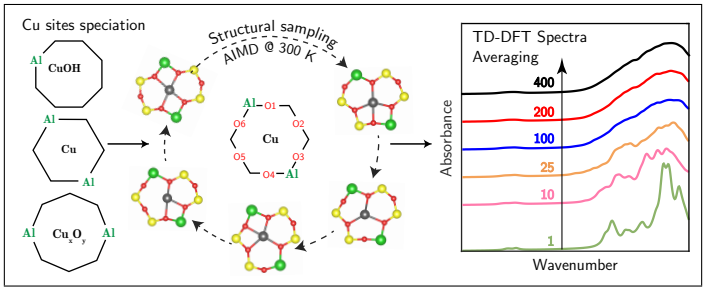

Supplement Information for: Consequences of Exchange-Site Heterogeneity and Dynamics on the UV-Visible Spectrum of Cu-Exchanged SSZ-13

Hui Li,[†,‖] Christopher Paolucci,[†,‡,‖] Ishant Khurana,[¶] Laura N. Wilcox,[¶] Florian Göltl,[§] Jonatan D. Albarracin Caballero,[¶] Arthur J. Shih,[¶] Fabio H. Ribeiro,[¶] Rajamani Gounder,[*,¶] and William F. Schneider[*,†]

†*Department of Chemical and Biomolecular Engineering, University of Notre Dame 182 Fitzpatrick Hall, Notre Dame, IN 46556, USA*

‡*Department of Chemical Engineering, University of Virginia, 102 Engineer's Way, Charlottesville, VA 22904, USA*

¶*Charles D. Davidson School of Chemical Engineering, Purdue University, 480 Stadium Mall Drive, West Lafayette, IN 47907, USA*

§*Department of Chemical and Biological Engineering, University of Wisconsin-Madison, 1415 Engineering Drive, Madison, WI 53706, USA*

‖*Contributed equally to this work*

E-mail: rgounder@purdue.edu; wschneider@nd.edu

Contents

S1 Computational Supplementary Information

To generate synthetic spectra, we used AIMD simulations at 300 K to generate a family of structures, TD-DFT calculations to compute excitation spectra at points along those trajectories, and averaging to generate composite spectra. Computational details are given below. For the computations reported here, approximately 20% of the total computational time is used in generating trajectories and 80% in computing the TD-DFT spectra.

	Machine types	
	EMSL (PNNL)	Notre Dame CRC
Processor specs	Intel Xeon processors, 128 GB memory per node, 16 cores per node, connected by FDR Infiniband network (https://www.emsl.pnl.gov/emslweb/instruments/computing-cascade-atipa-1440-intel-xeon-phi-node-fdr-infiniband-linux-cluster)	Intel Haswell processors, 256 GB RAM, 2 × 12 cores per node, connected by non Infiniband connection (https://wiki.crc.nd.edu/w/index.php/CRC_Quick_Start_Guide)
AIMD simulation hours	Each 150 ps AIMD simulation takes about 200 hours using 4 × 16 core machines	Each 150 ps AIMD simulation takes about 275 hours using 1 × 24 core machines
TD-DFT simulation hours	Each 3-step TD-DFT calculation (on one structure) takes about 1-2 hours using 1 × 16 core machines	Each 3-step TD-DFT calculation (on one structure) takes about 2-3 hours using 1 × 24 core machines

S1.1 AIMD computational details

We used the DFT-optimized geometries as initial structures to start the ab initio molecular dynamics (AIMD) simulations. Five independent simulations were performed non-spin-polarized at 300 K for 30 ps at 0.6 fs time step, for a total of 150 ps of AIMD. AIMD simulations for all Cu monomer and Cu dimer site structures are non-spin-polarized. We used the Car-Parrinello molecular dynamics software (CPMD)[1] to perform Born-Oppenheimer dynamics in the canonical (NVT) ensemble. Electron exchange and correlation were described by the generalized gradient approximation (GGA)[2,3] with Perdew-Becke-Erzenhof (PBE)

functional.[4] The ultrasoft Vanderbilt pseudopotential[5–7] was used with a cut off energy of 30 Rydberg (408 eV). The Nose-Hoover thermostat[8,9] was used to reach the target temperature of 300 K. The first Brillouin zone was sampled at the Γ-points only, for the insulator. Electronic energies were converged to 10^{-5} eV for each step of the AIMD. From each of the 5 independent 30 ps AIMD simulations, 12 ps was used for equilibration and 18 ps was used for data extraction.

S1.2 TD-DFT computational details

We used the TD-DFT method with a screened-hybrid exchange functional (HSE06)[10–14] to compute the UV-Vis absorbance spectrum. TD-DFT calculations were performed using the Vienna ab inito simulation package (VASP)[15] version 5.4.1, and the detailed methods are described in the next section. For Cu monomer structures (Z_2Cu para and meta, and ZCuOH) we performed the calculations with doublet spin state (ISPIN=2, NUPDOWN=1). For Cu dimer structures (Figure 4a in main text) we performed either singlet spin state calculations (ISPIN=2, NUPDOWN=0) or triplet spin state calculations (ISPIN=2, NUPDOWN=2), depending on the spin state of the lowest energy optimized geometry.

Using TD-DFT with a GGA functional predicts a close to zero band gap in Cu-SSZ-13 and an LMCT band from 0 to 20000 cm^{-1} (Figure S1). Optics calculation using HSE-generated wavefunctions without TDDFT results in a spectrum with no d-d transitions (Figure S1). A recent study by Ipek et al[16] used a combination of GW0 and BSE equation on HSE-computed wavefunctions, to compute UV-Vis spectrum of Cu(trans-μ-1,2-O_2)Cu and CuOCu dimer in SSZ-13, and obtained absorption peaks at similar energy levels as in Figure 4d. The differences in peak positions and intensities are likely due to the difference in method and the lack of spectrum averaging. This averaging is important because even the least mobile Z_2Cu species exhibit multiple modes of minima.

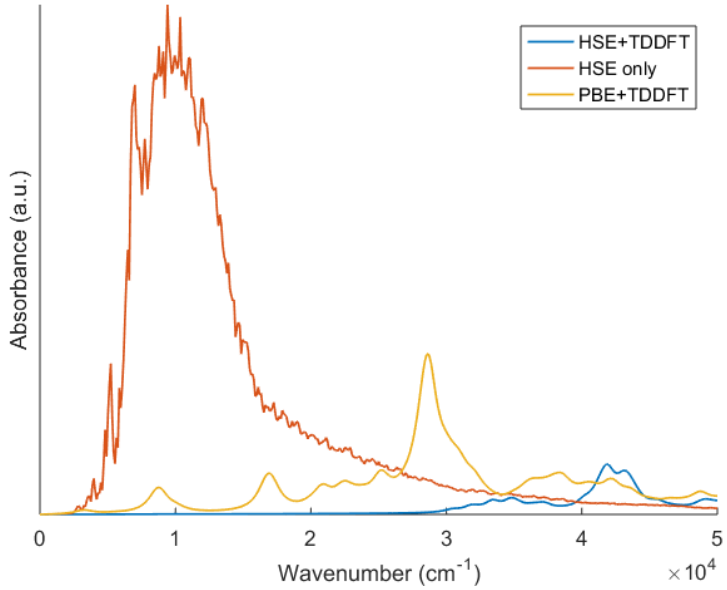

Figure S1: Comparison between UV-Vis spectra calculated at different levels of theory. The blue spectrum corresponds to the black spectrum in Figure 1d in the main text.

S1.2.1 Computational setup for the optical excitation calculations

Optical transitions were calculated using a Time-Dependent HF approach (casually referred to as TD-DFT throughout the manuscript) as implemented in the VASP[15] version 5.4.1. Here the optical response function (i.e. the frequency dependent dielectric function) including excitonic effects is calculated by solving the Casida equation.[17] In the calculations reported here an HSE type hybrid functional[10–14] with an exact exchange contribution of 40% was chosen as wave-function input. This value is close to the expected value for weakly screening materials and close to the value optimized for $CuCl_4$.[18] The calculations are a three step process. In the first step the wave functions for the system are calculated self consistently using the aforementioned functional for a small number of bands. Based on the input wave functions the Hamiltonian is furthermore diagonalized non-selfconsistently for a total of 3072 bands and corresponding wave functions and their derivatives are obtained. Finally optical transitions are calculated for 101 occupied and 200 unoccupied bands. Throughout all calculations energies were converged to differences smaller than 10^{-6} eV, the energy cut-

off was set to 417 eV and the spin states were fixed in the spin ground states of the modeled sites.

In a subsequent step we compared spectra obtained using the TD-DFT method with an HSE functional with 40% exchange to (a) linear response calculations using HSE inputs with 40% exact exchanged and (b) TD-DFT calculations with PBE as an input and (c) GW0 and BSE calculations reported in the literature.[16] Interestingly linear response calculations do not show a significant intensity for the d-d transitions (see Fig. S1). TD-DFT calculations using PBE as a functional significantly red-shift d-d transitions (see Fig. S1), a phenomenon also observed for GW0/BSE calculations in the literature.

S1.2.2 UV-Vis absorption calculation mathematical formula

Using the WAVECAR and WAVEDER files from the previous step, vasp calculates the frequency dependent dielectric matrix ($D(\nu)$) at discrete energy (ν) intervals of 121 cm^{-1} from 0 to 121,000 cm^{-1}. At each energy level (ν) the absorption ($\eta(\nu)$) is then computed to obtain the real (A_{real}) and imaginary (A_{imag}) components of the dielectric matrix ($D(\nu)$). To visualize the UV-Vis absorption, we spline together the $\eta(\nu)$ values at each discrete ν to form a continuous spectrum. η is dimensionless and quatitatively meaningful; it is analogous to units of Kubelka-Munk (K.M.).

$$A_{\text{real}} = \frac{tr\Big(diag\big(real(D)\big)\Big)}{3} \tag{1}$$

$$A_{\text{imag}} = \frac{tr\Big(diag\big(imag(D)\big)\Big)}{3} \tag{2}$$

$$\eta = imag\Big(\sqrt{A_{\text{real}} + iA_{\text{imag}}}\Big) \tag{3}$$

S1.2.3 UV-Vis spectrum calculation and plotting script

This script assumes that there are 400 individual TD-DFT calculations, where 400 real and imaginary dielectric response matrices are extracted from the vasprun.xml files, and placed under folders “real" and “img" respectively.

```
clear all
N=400;
nonzeroentries=N;
aa=[1:1:N];
for ii=1:size(aa,2)
    ranges{ii}=aa(ii);
end
for i=1:N
    dd1=sprintf('img/img%d',ranges{i});
    A1=importdata(dd1);
    dd2=sprintf('real/real%d',ranges{i});
    A2=importdata(dd2);
    if isempty(A1)
        nonzeroentries=nonzeroentries-1;
        continue
    else
        E=A1(:,1);
        Eev=E.*8065.73;
        for j=1:size(A1,1)
            M(1,1)=A1(j,2); M(1,2)=A1(j,5); M(1,3)=A1(j,7);
            M(2,1)=A1(j,5); M(2,2)=A1(j,3); M(2,3)=A1(j,6);
            M(3,1)=A1(j,7); M(3,2)=A1(j,6); M(3,3)=A1(j,4);
            mm(j,1)=sum(diag(M))/3;
        end
        for j=1:size(A1,1)
            R(1,1)=A2(j,2); R(1,2)=A2(j,5); R(1,3)=A2(j,7);
            R(2,1)=A2(j,5); R(2,2)=A2(j,3); R(2,3)=A2(j,6);
            R(3,1)=A2(j,7); R(3,2)=A2(j,6); R(3,3)=A2(j,4);
            rr(j,1)=sum(diag(R))/3;
        end
        tt=imag(sqrt(rr+mm*1i));
        AB(:,i)=tt;
    end
end
Abs=sum(AB,2)./nonzeroentries;
figure;
plot(Eev,Abs);
axis([0 50000 0 -Inf Inf]);
xlabel('Wavenumber (cm^-^1)');
ylabel('Absorbance (a.u.)');
```

S1.3 Calculated Z_2Cu para and meta minima energies

Table S1: Relative energies of the 6 minimum energy structures for Z2Cu.

Al-Al configuration	Minima	Energy (kJ mol^{-1}), relative to lowest energy in all 6 minima	Energy (kJ mol^{-1}), relative to lowest energy in each Al-Al
para	1	5.3	5.3
3NN Al-Al (Fig. 1a)	2	0.0	0.0
	3	0.6	0.6
meta	1	37.3	12.7
2NN Al-Al (Fig. 1f)	2	24.6	0.0
	3	45.1	20.5

S1.4 Cu$-O_f$ distance distributions

Table S2: Cu$-O_f$ distances means and standard deviations (Å) for the histogram analysis in Fig. 2b, Fig. 2f, and Fig 3b.

	first		second	
	Mean (Å)	Standard deviation (Å)	Mean (Å)	Standard deviation (Å)
Z2Cu para (Fig. 2b)	2.08	0.11	3.31	0.15
Z2Cu para (Fig. 2f)	2.09	0.12	3.33	0.16
ZCuOH (Fig. 3b)	1.77	0.04	2.01	0.08

S1.5 Example of intermediate state structure

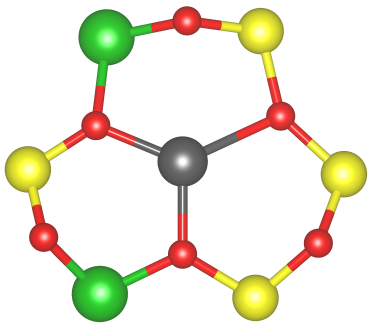

Figure S2: Example of a Z_2Cu meta structure from one of the 400 AIMD snapshots where Cu is only bonded to three first-shell O_f in the 6MR, and does not belong to any of the local minima modes shown in Figure 1e. Structures like this are shown as the white slice in Figure 1f pie chart inset.

S1.6 Boltzmann weighting of spectra

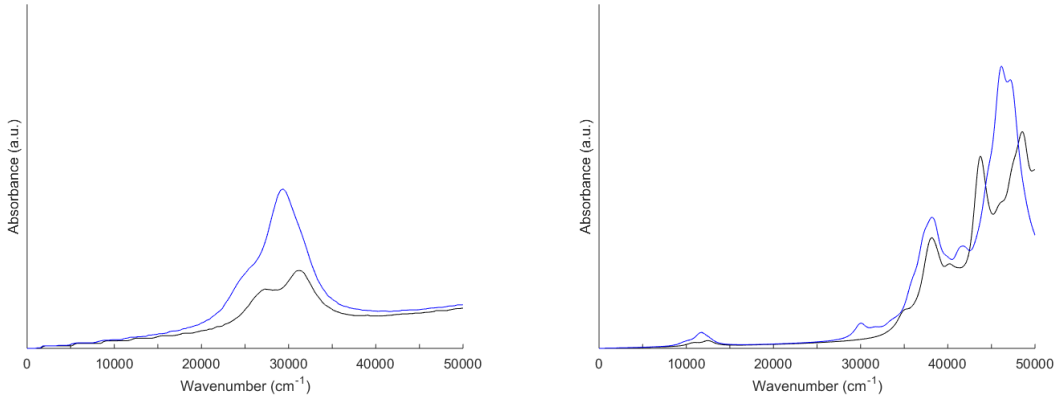

Figure S3: Boltzmann weighted UV-Vis spectra for Z_2Cu para (black) and meta (blue), using the simulated spectra of the 3 minima respectively (Fig. 2c and 2g in the main text). Left panel shows the d-d transition region and the right panel shows the LMCT region.

S1.7 Overlaid 400 UV-Vis spectra

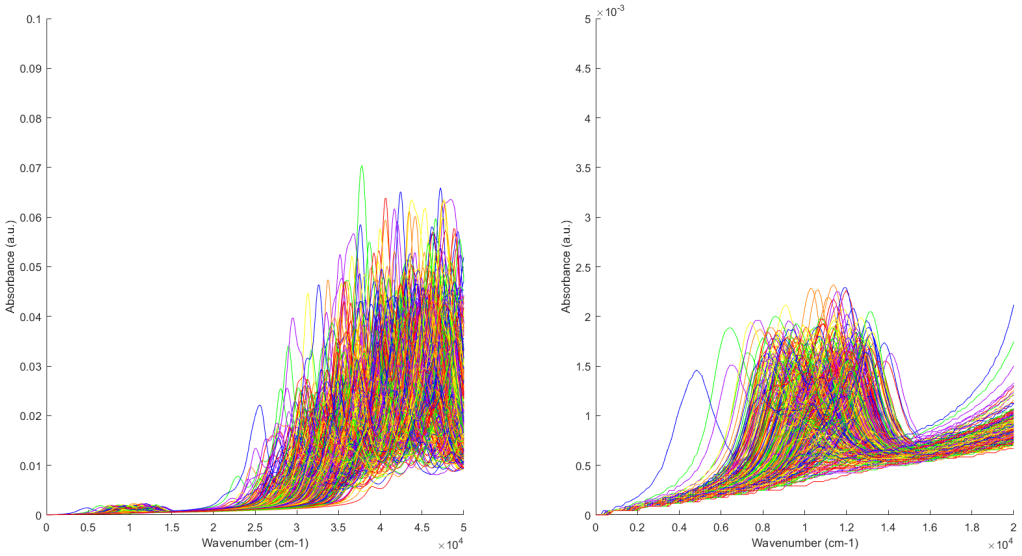

(a) Z_2Cu para

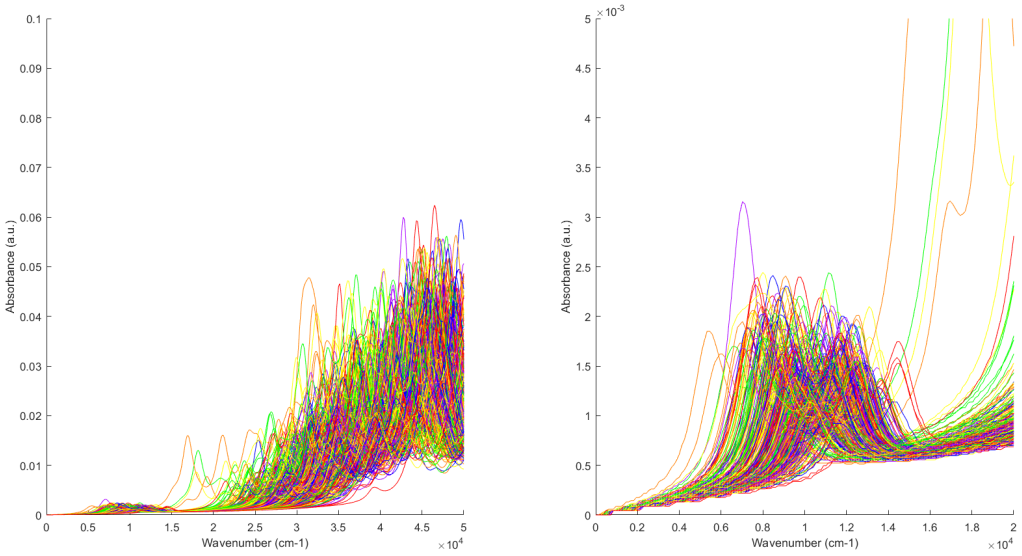

(b) Z_2Cu meta

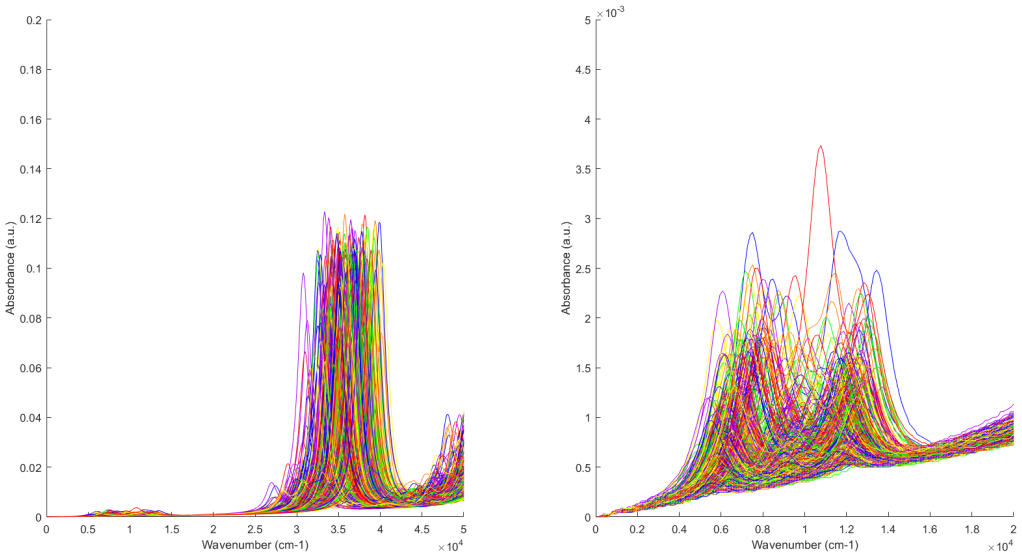

(c) ZCuOH

Figure S4: Overlay of 400 UV-Vis spectra used for averaging, left figures show the 0 to 50,000 cm^{-1} range and the right figures show the 0 to 20,000 cm^{-1} range.

S1.8 d-d transition energy relative to the Cu−O_f distances

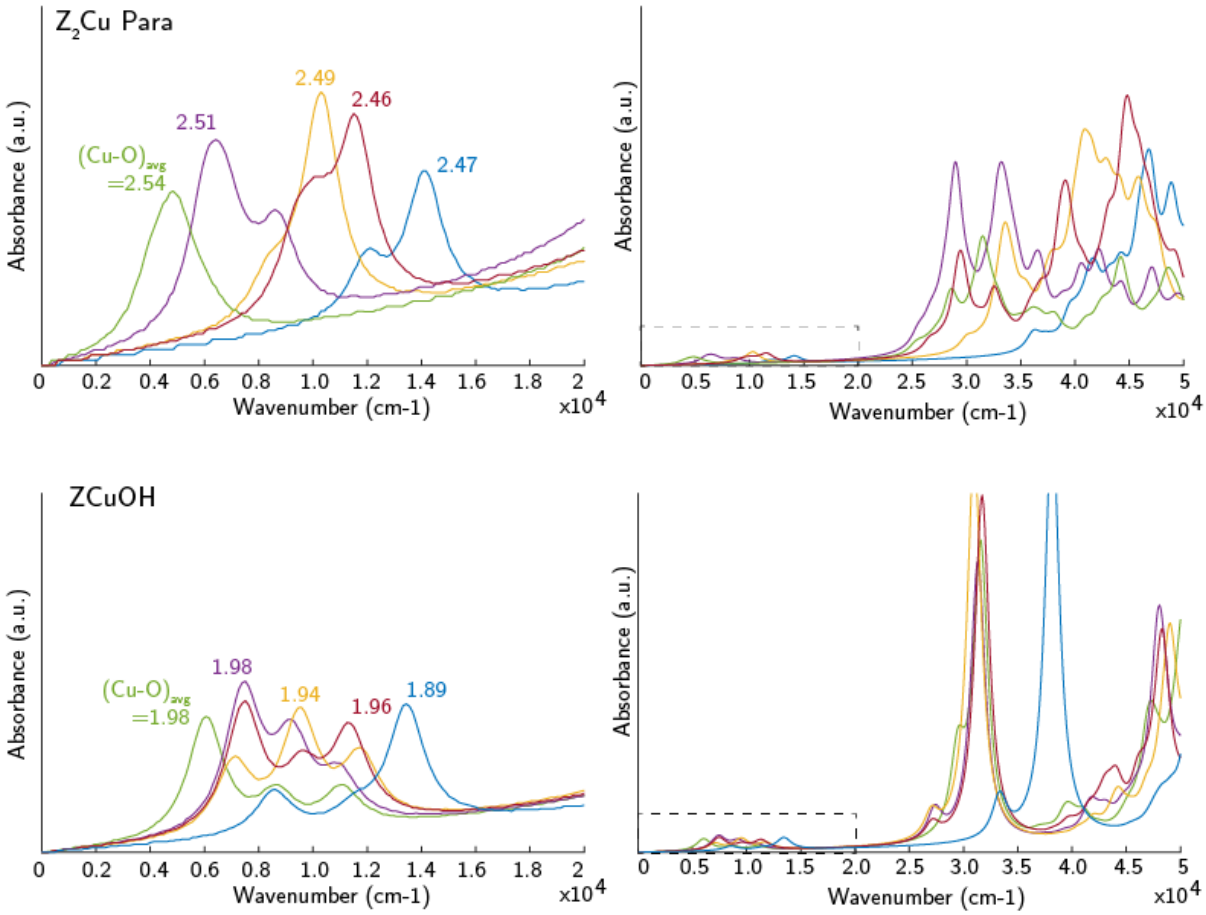

Figure S5: Five representative Z_2Cu para, and ZCuOH UV-Vis spectra from 5 snapshots in the AIMD and the averaged Cu-O distances for each snapshot. Cu-O averages are calculated using the 6 Cu−O_f distances in the Z_2Cu para case, and 2 Cu−O_f plus Cu-O(H) distances in the ZCuOH case. In general the longer the average Cu-O bonds the smaller the d-d transition wavenumber, vice versa.

S1.9 RDF of the 8MR ZCuOH

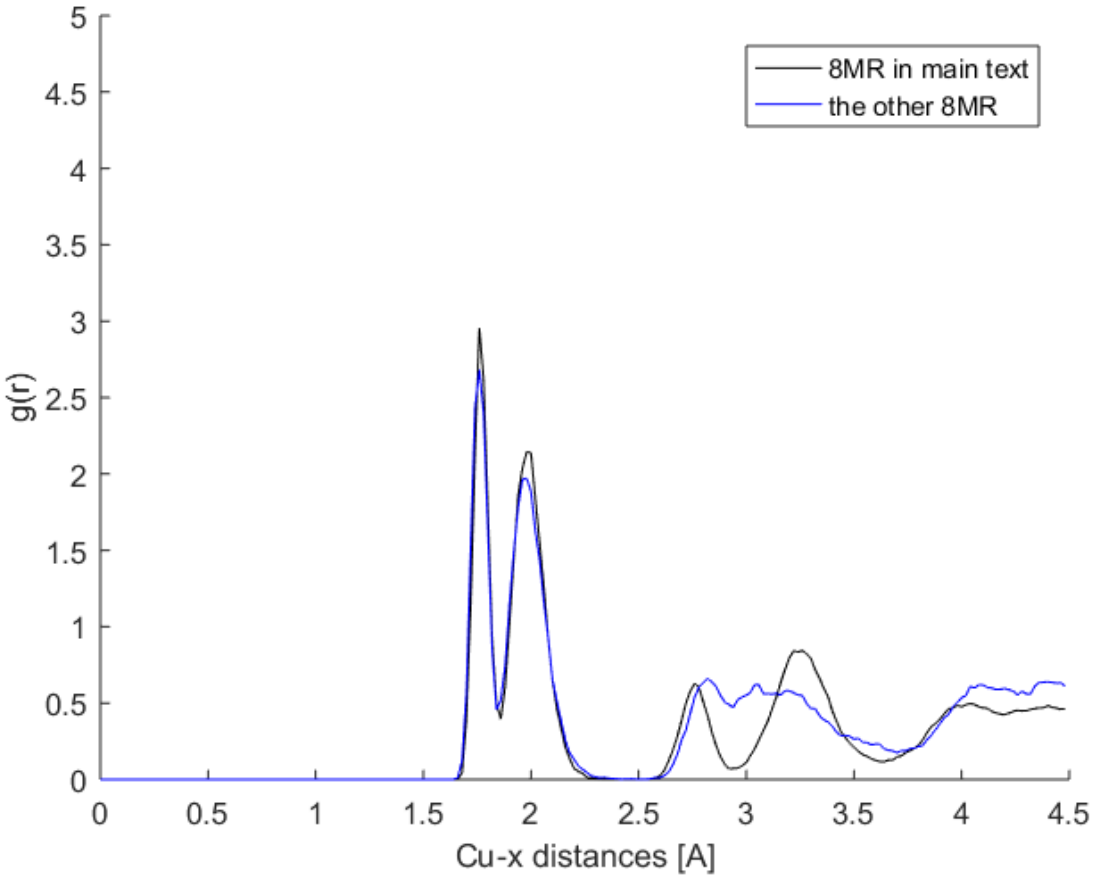

Figure S6: Computed RDF from 150 ps of 300 K AIMDs, for the two different 8MR ZCuOH configurations with the same Al T-site.

S1.10 NEB calculation for $[CuOH]^+$ migration barrier

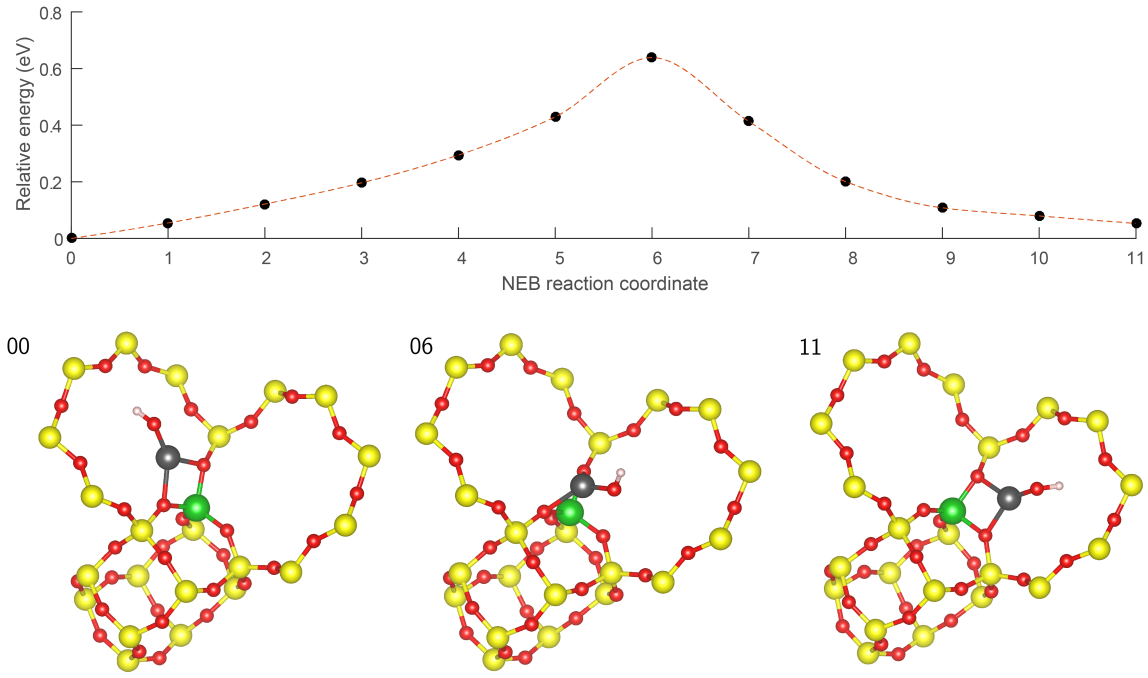

Figure S7: Top: Nudge elastic band (NEB) calculated energy barrier of CuOH switching coordination from one 8MR to an adjacent 8MR. Red dotted curve is the spline interpolation between the relative energy data points and is used only as a guide to eyes. Bottom: Starting (00), transition (06), and ending (11) structures from NEB snapshot images.

S1.11 ZCuO UV-Vis spectrum

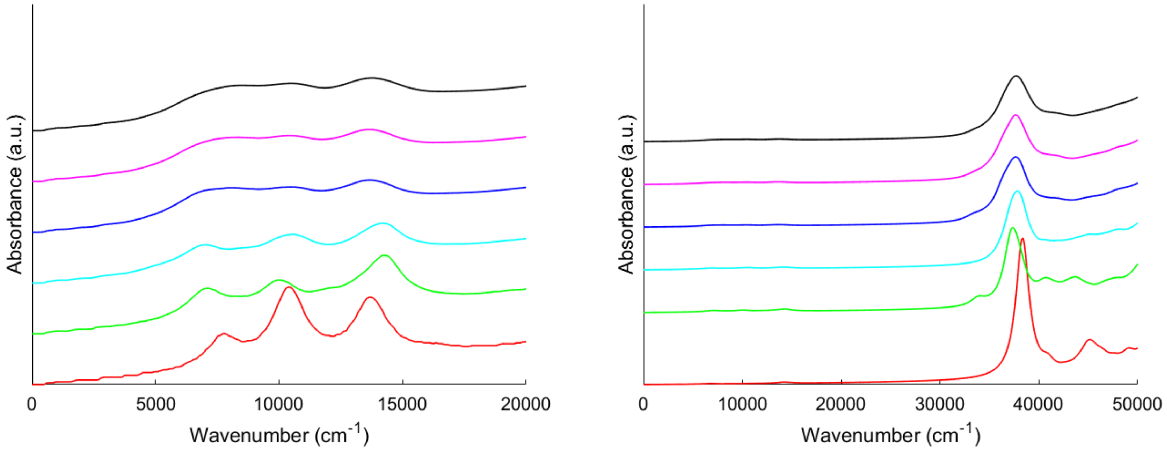

Figure S8: UV-Vis spectrum of ZCuO at 300 K, averaged with 1 (red), 10 (green), 25 (cyan), 100 (blue), 200 (magenta), and 400 (black) structures.

S1.12 Condensation of 2 proximal ZCuOH

To estimate the temperature and water concentration where the two condensation reactions are favorable, we constructed a thermodynamic phase diagram, computed under the same assumptions (Figure S10). Energies were taken from DFT calculated energies in 36-T super-cells. The harmonic vibrator approximation was used for formation entropy, and reference chemical potential of H_2O is read from the JANAF table. Condensation to the dihydroxyl dimer $ZCu(OH)_2CuZ$ (Eqn 1) is more favorable at T $<$ 350 K (H_2O =5% -7%), while the CuOCu dimer (Eqn 2) becomes more exergonic above 350 K. Two $[CuOH]^+$ across an 8MR are thus expected to exist as dimers over a wide range of conditions.

$$2\,\mathrm{ZCuOH} \longrightarrow \mathrm{ZCu(OH)_2CuZ} \tag{4}$$

$$2\,\mathrm{ZCuOH} \longrightarrow \mathrm{ZCuOCuZ} + \mathrm{H_2O} \tag{5}$$

Table S3: Computed PBE-D2 energies of the two reactions above.

Reaction	Energy, singlet (kJ mol^{-1})	Energy, triplet (kJ mol^{-1})
(4)	-96.2	-108.7
(5)	46.8	35.3

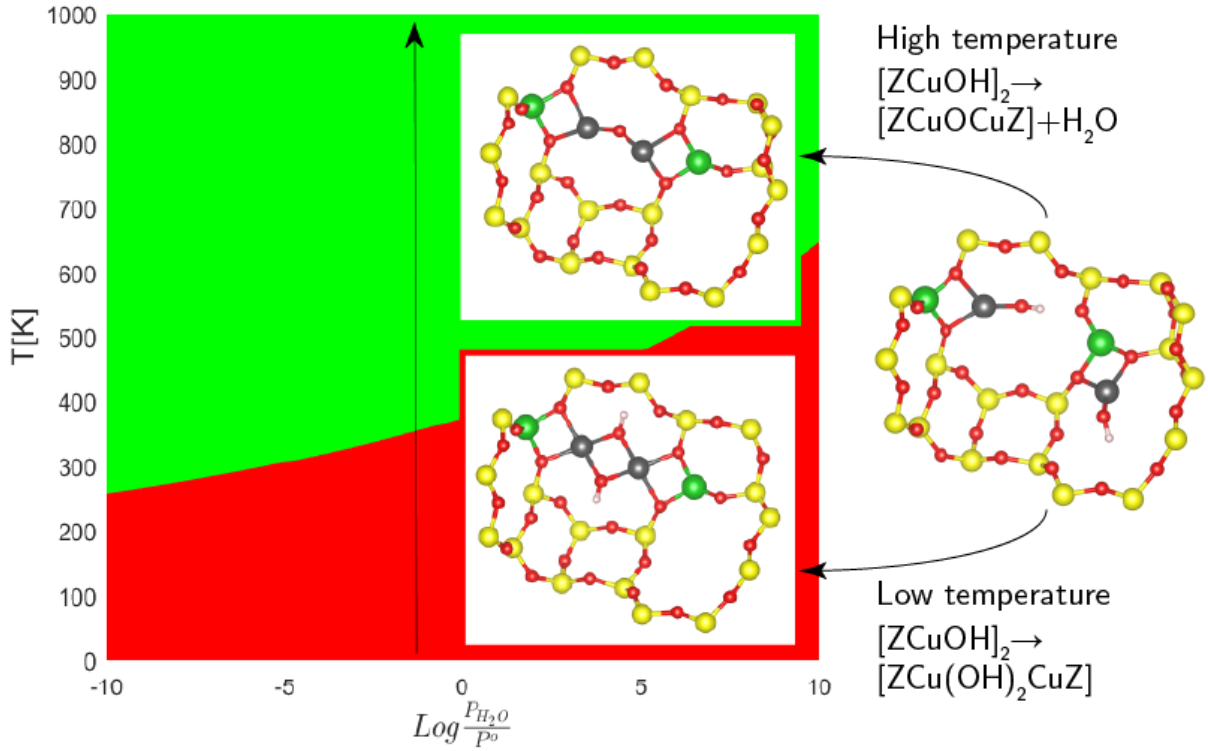

Figure S9: Phase diagram of free energy of formation between ZCuOCuZ ($+H_2O$) and $ZCu(OH)_2CuZ$ dimer species, plotted with respect to temperature and P_{H_2O}.

S1.13 Spectra averaging for dimers A-G

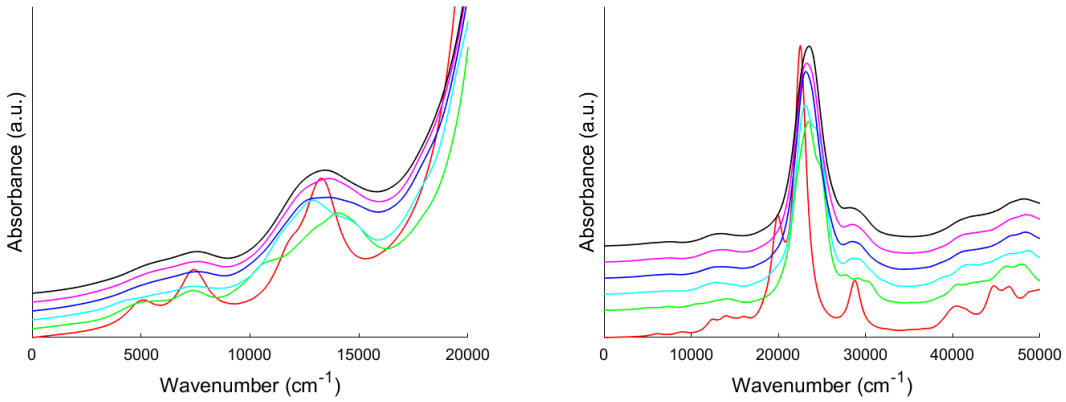

(a) Dimer A

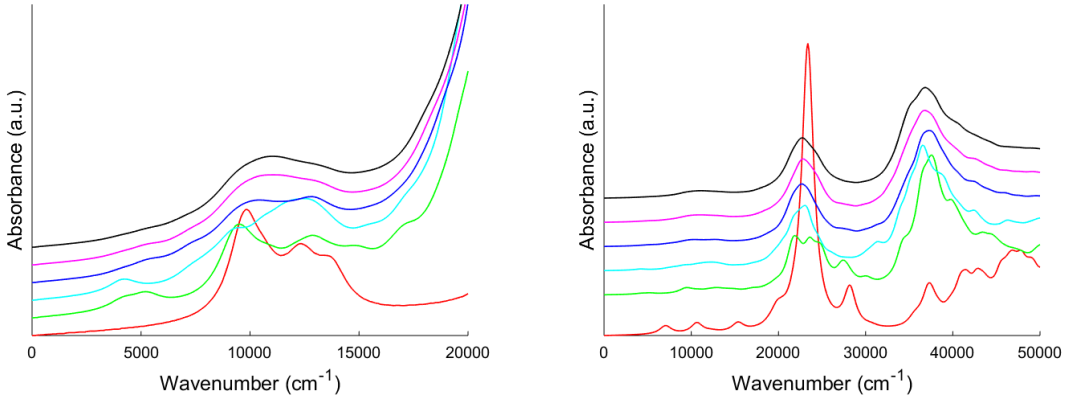

(b) Dimer B

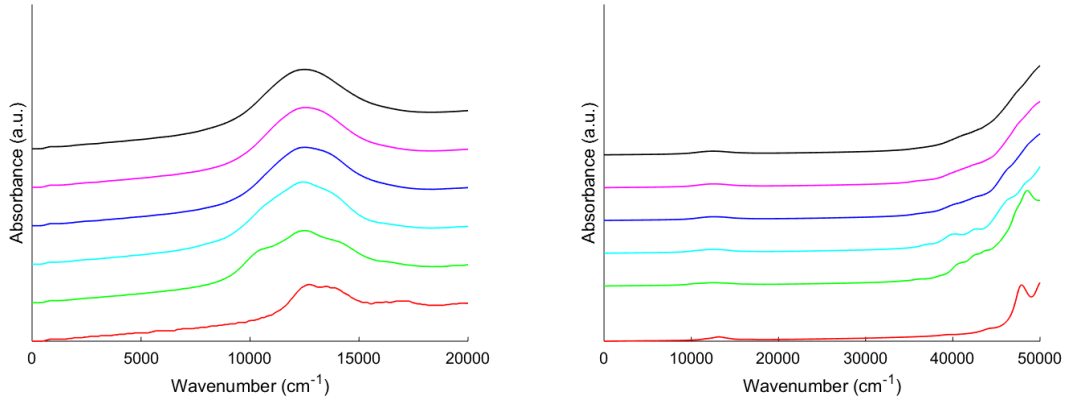

(c) Dimer C

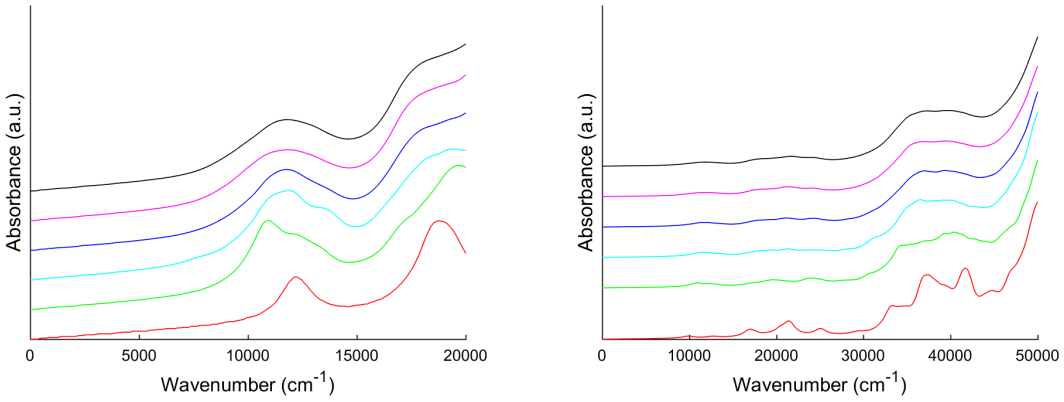

(d) Dimer D

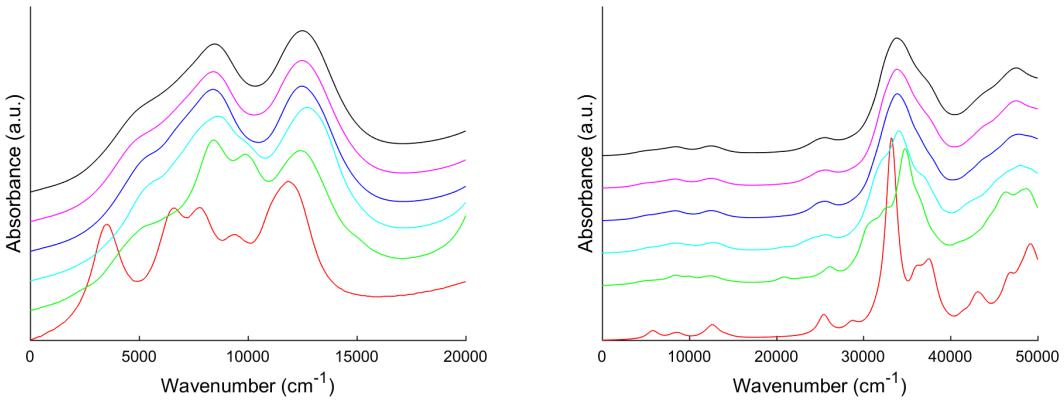

(e) Dimer E

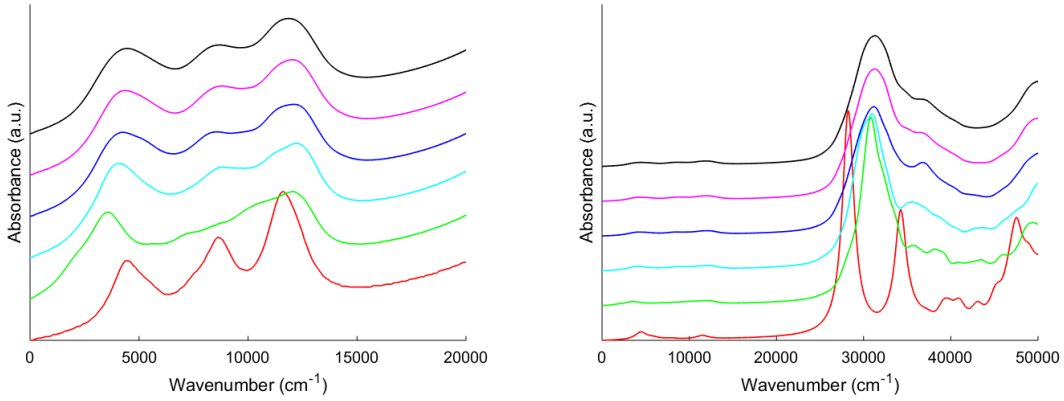

(f) Dimer F

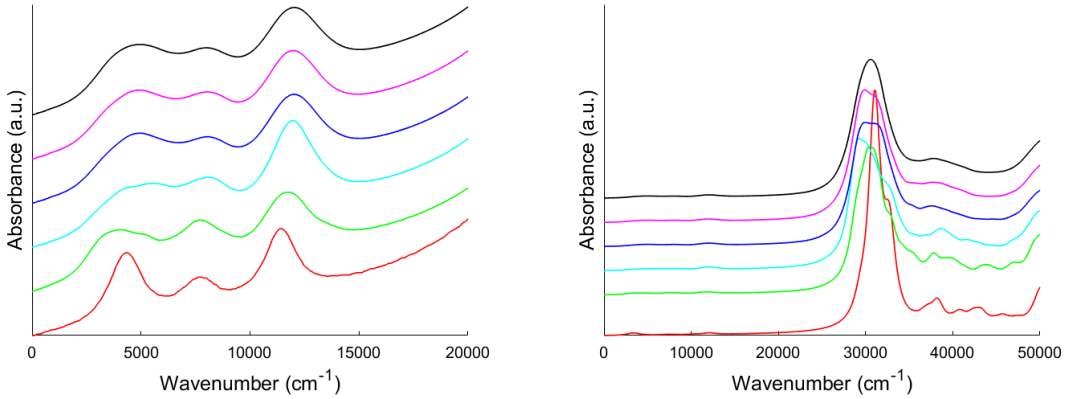

(g) Dimer G

Figure S10: UV-Vis spectrum averaging for dimers in Fig. 4a A-G, with 1 (red), 10 (green), 25 (cyan), 100 (blue), 200 (magenta), and 400 (black) structures, left figures show the 0 to 20,000 cm^{-1} range and the right figures show the 0 to 50,000 cm^{-1} range.

S1.14 Dimer B energy minima

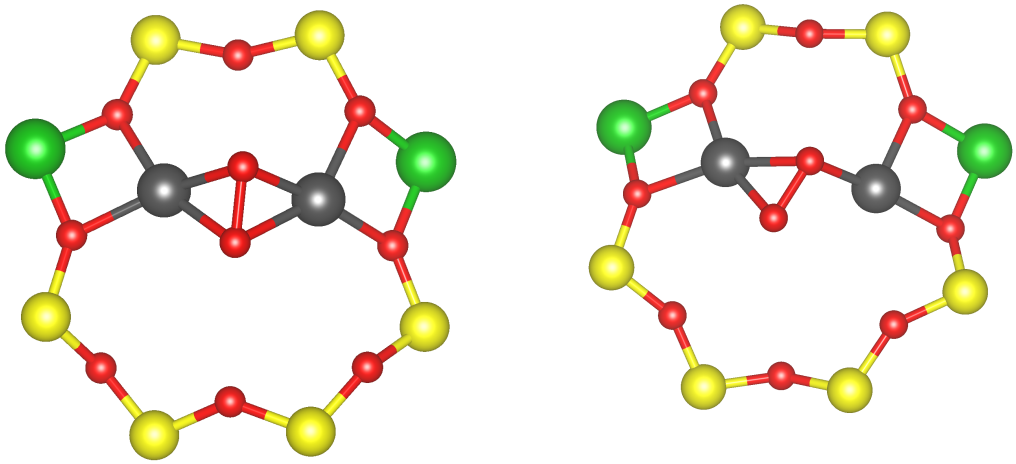

(a) (b)

Figure S11: The two energy local minima structures for dimer B, (a) the lower energy minima, the same as presented in Fig. 4a, (b) the local minima 7 kJ mol higher in energy than (a).

S1.15 Dimer C geometry

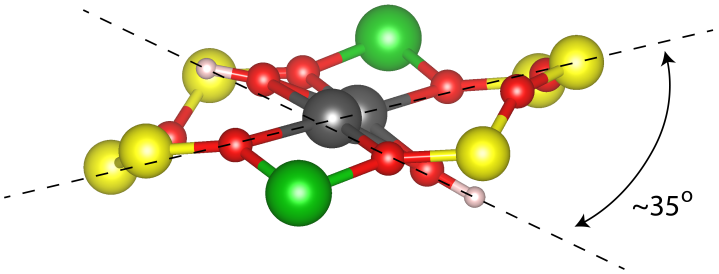

Figure S12: The ≈ 35° angle between the plane of the 8MR and the plane of the $Cu(OH)_2Cu$ core.

S1.16 Dimer A geometry

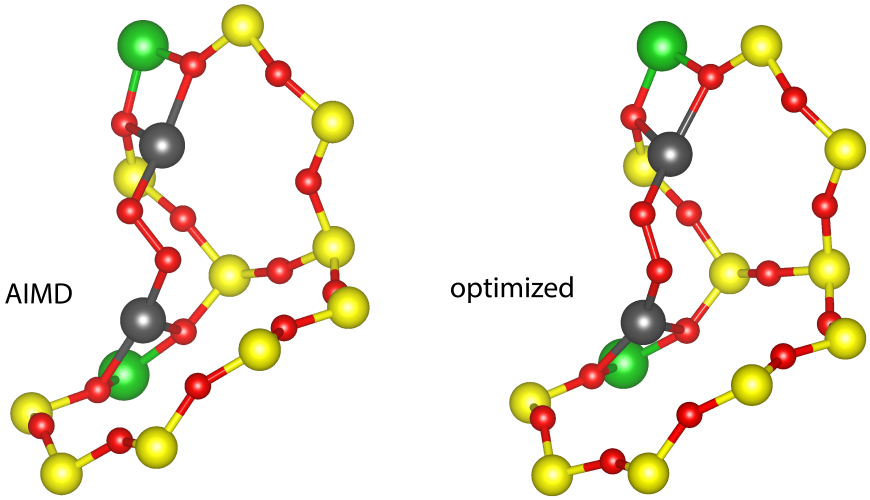

Figure S13: (left) Representative structure of dimer A during AIMD (with smaller Cu-O-O angle). (right) The optimized structure of dimer A.

S2 Experimental Supplementary Information

S2.1 Sample preparation

S2.1.1 Synthesis of SSZ-13 with Si/Al=5

SSZ-13 with Si/Al of 5 was synthesized from a conversion of FAU to CHA with the addition of N,N,N-trimethyl-1-adamantylammonium hydroxide (TMAdaOH) using a method developed by Zones[19] and modified by Fickel.[20] The molar ratios used for the synthesis were 1 SiO_2 / 0.031 Al_2O_3 / 0.77 Na_2O / 0.017 TMAdaOH / 12.1 H_2O. A typical synthesis included the addition of 3.14 g of a 1 M NaOH solution (3.3 wt% NaOH, Alfa Aesar) to 4.82 g of deionized water (18.2 MΩ) and allowed to stir for 0.25 h. Next 24.1 g of sodium silicate (25.6 wt% SiO2, 10.6 wt% Na_2O, Sigma Aldrich) were added to the PFA jar and homogenized for 0.25 h, followed by the addition of 0.37 g of NH4-Y with Si/Al = 2.6 (CBV300, Zeolyst) with additional mixing for 0.5 h. Then 1.58 g of 1 M TMAdaOH (25 wt%, Sachem) were added to the mixture and homogenized for 0.5 h. The solution was stirred under ambient conditions throughout the entire synthesis. The synthesis gel was loaded into 45 ml Teflon liners, encased in stainless steel autoclaves (Parr Instruments), and held at 413 K for 6 days under rotation at 60 RPM in a forced convection oven (Yamato DKN-402C).

S2.1.2 Synthesis of SSZ-13 with Si/Al=15

For the synthesis of SSZ-13 with isolated Al distribution, only $TMAda^+$ was used as a charge balancing cation. To achieve Si/Al of 15, molar ratios of 1 SiO_2 / 0.033 Al_2O_3 / 0.50 TMAdaOH / 44 H_2O were used. In a representative synthesis, 14.07 g of 1 M TMAdaOH solution (25 wt%, Sachem) were added to 12.841 g of deionized water (18.2 MΩ) in a PFA jar and allowed to stir for 0.25 h. Then 0.173 g of $Al(OH)_3$ (98 wt%, SPI Pharma) were added to the PFA jar and homogenized for 0.25 h. Next 5 g of colloidal silica (LudoxHS40, 40 wt%, Sigma Aldrich) were added to the solution and stirred for 2 h. The synthesis solution remained under ambient conditions during the addition and homogenization process. The

synthesis gel was loaded into 45 ml Teflon liners, encased in stainless steel autoclaves (Parr Instruments), and held at 433 K for 6 days under rotation at 40 RPM in a forced convection oven (Yamato DKN-402C).

S2.1.3 Copper Exchange Protocol

The H-form zeolites were copper exchanged using aqueous-phase ion exchange with 0.001 M - 0.1 M $Cu(NO_3)_2$ solution (100 cm^3 g $catalyst^{-1}$; Sigma Aldrich, 99.999 wt%) at ambient conditions for 4 h. The exchange was pH controlled for 4.9 $\pm$ 0.1 with dropwise addition of 1 M NH_4OH (Sigma Aldrich). After exchange, the zeolites were recovered by centrifugation and washed with deionized water six times, dried at 373 K, and then treated in flowing dry air (1.67 cm^3 s^{-1} g $catalyst^{-1}$, 99.999% UHP, Indiana Oxygen) to 773 K (0.0167 K s^{-1}) for 4 h. Elemental analysis was determined using atomic absorption spectroscopy (AAS) with a PerkinElmer AAnalyst 300. Al was measured in a reducing acetylene and nitrous oxide flame at the wavelength 309.3 nm; Cu was measured at the wavelength 324.8 nm in an oxidizing air and acetylene flame. The samples were prepared by dissolving 20 mg of zeolite in 2 g of hydrofluoric acid (48 wt%, Sigma Aldrich), followed by a dilution with 50 g of deionized water.

S2.2 UV-Vis spectroscopy

Diffuse reflectance UV-Visible spectra were recorded under various gas conditions using a Varian UV-VIS-NIR spectrophotometer (Cary 5000) with a diffuse reflectance accessory consisting of two ellipsoidal mirrors (Harrick Scientific Praying Mantis). Barium sulfate (BaSO4, 99.9%, Sigma-Aldrich) was used as the 100% reflectance standard. An in-situ sample holder was loaded with 0.1 g of sample, which was pelleted and sieved to retain particles between 180-250 μm in diameter. Spectra were collected from 7000 to 50000 cm^{-1} with a scan speed of 33.33 cm^{-1} s^{-1}.

S2.3 High temperature O_2 treatment

The sample was dehydrated at 673 K (temperature ramp of 0.5 K s^{-1}) in oxidizing atmosphere of dry air (commercial grade, Indiana Oxygen) with a total flow of 0.833 cm^3 s^{-1} and held at temperature for 2 h. The sample was then cooled to 473 K under the same oxidizing atmosphere, and was further allowed to cool to 300 K. Sample spectra were collected during the cooling steps at 473 K and 300 K.

S2.4 CO reducing treatment

After exposing to high temperature oxidative conditions (673 K in dry air, 2 h), the sample was reduced with 5% CO in balance He (99.999% UHP, Indiana Oxygen) with a total flow of 0.833 cm^3 s^{-1} at 523 K (temperature ramp of 0.5 K s). The sample was exposed to CO until the collected spectra stopped changing, indicating steady state or complete reduction with CO. Then, the sample was flushed with inert He (99.999% UHP, Indiana Oxygen) at 523 K for 0.5 h to remove any physisorbed CO and was further allowed to cool down to 300 K in He flow. The sample spectra were collected during cooling at 473 K and 300 K.

S2.5 Additional table

Table S4: Bulk elemental analysis and fraction of Z_2Cu/ZCuOH sites on the three Cu-SSZ-13 samples.

Type of Cu sites	Si/Al	Cu/Al	Cu wt%	Z2Cu/total Cu	ZCuOH/total Cu
Z2Cu site	5	0.21	3.7	0.21	0.00
ZCuOH site	15	0.24	1.7	0.00	0.24
	15	0.15	1.0	0.00	0.15

References

(1) IBM Corporation, Carr-Parrinello Molecular Dynamics Code, copyright IBM Corp 1990–2016, copyright MPI für Festkörperforschung Stuggart 1997–2001. 2016; `http:`

//www.cpmd.org/.

(2) Perdew, J. P.; Chevary, J. A.; Vosko, S. H.; Jackson, K. A.; Pederson, M. R.; Singh, D. J.; Fiolhais, C. Atoms, molecules, solids, and surfaces: Applications of the generalized gradient approximation for exchange and correlation. *Phys. Rev. B* **1992**, *46*, 6671–6687.

(3) Perdew, J. P.; Burke, K.; Ernzerhof, M. Generalized Gradient Approximation Made Simple. *Phys. Rev. Lett.* **1997**, *78*, 1396.

(4) Perdew, J. P.; Wang, Y. Accurate and Simple Analytic Representation of the Electron-Gas Correlation-Energy. *Phys. Rev. B* **1992**, *45*, 13244–13249.

(5) Vanderbilt, D. Soft self-consistent pseudopotentials in a generalized eigenvalue formalism. *Phys. Rev. B* **1990**, *41*, 7892–7895.

(6) Laasonen, K.; Car, R.; Lee, C.; Vanderbilt, D. Implementation of ultrasoft pseudopotentials in ab initio molecular dynamics. *Phys. Rev. B* **1991**, *43*, 6796–6799.

(7) Laasonen, K.; Pasquarello, A.; Car, R.; Lee, C.; Vanderbilt, D. Car-Parrinello molecular dynamics with Vanderbilt ultrasoft pseudopotentials. *Phys. Rev. B* **1993**, *47*, 10142–10153.

(8) Nosé, S. A unified formulation of the constant temperature molecular dynamics methods. *J. Chem. Phys.* **1984**, *81*, 511–519.

(9) Hoover, W. G. Canonical dynamics: Equilibrium phase-space distributions. *Phys. Rev. A* **1985**, *31*, 1695–1697.

(10) Heyd, J.; Scuseria, G. E.; Ernzerhof, M. Hybrid functionals based on a screened Coulomb potential. *J. Chem. Phys.* **2003**, *118*, 8207–8215.

(11) Heyd, J.; Scuseria, G. E. Efficient hybrid density functional calculations in solids: Assessment of the Heyd-Scuseria-Ernzerhof screened Coulomb hybrid functional. *J. Chem. Phys.* **2004**, *121*, 1187–1192.

(12) Heyd, J.; Peralta, J. E.; Scuseria, G. E.; Martin, R. L. Energy band gaps and lattice parameters evaluated with the Heyd-Scuseria-Ernzerhof screened hybrid functional. *J. Chem. Phys.* **2005**, *123*, 174101.

(13) Heyd, J.; Scuseria, G. E.; Ernzerhof, M. Erratum:âĂIJHybrid functionals based on a screened Coulomb potentialâĂİ[J. Chem. Phys. 118, 8207 (2003)]. *J. Chem. Phys.* **2006**, *124*, 219906.

(14) Krukau, A. V.; Vydrov, O. A.; Izmaylov, A. F.; Scuseria, G. E. Influence of the exchange screening parameter on the performance of screened hybrid functionals. *J. Chem. Phys.* **2006**, *125*, 224106.

(15) Vienna ab-initio Software Package. `www.vasp.at`.

(16) Ipek, B.; Wulfers, M. J.; Kim, H.; Göltl, F.; Hermans, I.; Smith, J. P.; Booksh, K. S.; Brown, C. M.; Lobo, R. F. Formation of [Cu2O2]2+ and [Cu2O]2+ toward C-H Bond Activation in Cu-SSZ-13 and Cu-SSZ-39. *ACS Catal.* **2017**, *7*, 4291–4303.

(17) Casida, M. E. Generalization of the optimized-effective-potential model to include electron correlation: A variational derivation of the Sham-Schlüter equation for the exact exchange-correlation potential. *Phys. Rev. A* **1995**, *51*, 2005–2013.

(18) Szilagyi, R. K.; Metz, M.; Solomon, E. I. Spectroscopic Calibration of Modern Density Functional Methods Using [CuCl4]2-. *The Journal of Physical Chemistry A* **2002**, *106*, 2994–3007.

(19) Zones, S. I. Conversion of faujasites to high-silica chabazite SSZ-13 in the presence of

N{,}N{,}N-trimethyl-1-adamantammonium iodide. *J. Chem. Soc.{,} Faraday Trans.* **1991**, *87*, 3709–3716.

(20) Fickel, D. W.; Lobo, R. F. Copper coordination in Cu-SSZ-13 and Cu-SSZ-16 investigated by variable-temperature XRD. *J. Phys. Chem. C* **2010**, *114*, 1633–1640.